TEMPO Nitrogen Dioxide Retrieval Algorithm Theoretical Basis Document

Caroline R. Nowlan[1], Gonzalo González Abad[1], Xiong Liu[1], Huiqun Wang[1] and Kelly Chance[1]

[1]Center for Astrophysics | Harvard & Smithsonian

Corresponding author: Caroline R. Nowlan (cnowlan@cfa.harvard.edu)

VERSION	v1.0
RELEASE DATE	February 1, 2025
KEYWORDS	NITROGEN DIOXIDE NITROGEN OXIDES TEMPO AIR QUALITY ATMOSPHERIC CHEMISTRY
REVIEWERS	Laura Judd (NASA LaRC) Lok Lamsal (NASA GSFC, UMBC)
DOI	10.5067/WX026254FI2U

This document should be cited as:
Nowlan, C. R., González Abad, G., Liu, X., Wang, H., & Chance, K. (2025). TEMPO Nitrogen Dioxide Retrieval Algorithm Theoretical Basis Document. NASA Algorithm Publication Tool, https://doi.org/10.5067/WX026254FI2U.

Table of Contents

Abstract

This Algorithm Theoretical Basis Document (ATBD) describes the retrieval algorithm and product details for the Level 2 nitrogen dioxide (NO_2) product from the Tropospheric Emissions: Monitoring of Pollution (TEMPO) satellite instrument. TEMPO is the first air quality mission dedicated to measuring atmospheric trace gases and aerosols over North America from geostationary orbit. The NO_2 product is produced using a three-step process. First, the retrieval algorithm derives the slant column density of NO_2 from backscattered solar light. Second, the algorithm calculates tropospheric and stratospheric air mass factors that describe the light path through NO_2 in the atmosphere. In the third step, the algorithm uses the observed slant columns, air mass factors and ancillary information to separate the stratospheric and tropospheric components of the NO_2 columns and to determine tropospheric and stratospheric vertical column densities. The ATBD describes the TEMPO version 3 NO_2 data product's retrieval algorithm, algorithm inputs and outputs, validation and practices for best use.

Plain Language Summary

TEMPO (Tropospheric Emissions: Monitoring of Pollution) is a satellite mission in geostationary orbit that measures trace gases, clouds and aerosols of importance to air quality. This document describes the retrieval algorithm and product details for the TEMPO Level 2 nitrogen dioxide (NO_2) product.

Version Description

This is Version 1.0 (initial release) of the TEMPO nitrogen dioxide ATBD. This document was initially released under DOI old-10.5067/8YMVQJZZP6S2 from February 1 to March 20, 2025, but has been updated to DOI 10.5067/WX026254FI2U. References to DOI old-10.5067/8YMVQJZZP6S2 should be updated to reflect this new DOI.

1. Introduction

1.1. TEMPO Overview

TEMPO is NASA's first Earth Venture Instrument (EVI-1) project, selected in 2012. It is a PI-led instrument project at the Smithsonian Astrophysical Observatory (SAO) with project management at NASA Langley Research Center (LaRC) and instrument development at Ball Aerospace (now BAE Systems). TEMPO is NASA's first payload to be hosted on a commercial spacecraft. After the TEMPO instrument delivery in November 2018, the TEMPO mission partnered with the satellite provider Maxar in 2019 and the host Intelsat in 2020. The TEMPO instrument was launched on April 7, 2023 on board the commercial communication satellite Intelsat-40e (IS-40e) by a SpaceX Falcon 9 rocket into a geostationary orbit at 91° W. TEMPO's first direct Sun observation took place on August 1, 2023, followed by the first Earth-view observations on August 2, 2023. TEMPO began nominal operations on October 17, 2023.

TEMPO uses the UV/visible spectroscopic technique to measure atmospheric pollution across North America, from Mexico City/Puerto Rico to the Canadian oil sands, and from the Atlantic to the Pacific, hourly and at high spatial resolution. Measurements are made from geostationary orbit, which allows for nearly continuous daylight monitoring to capture the inherent high temporal variability in pollutants due to emissions, chemistry and meteorology. TEMPO's small spatial footprint resolves pollution sources at a sub-urban scale.

TEMPO measures the spectra required to retrieve the mission baseline data products of total and profile ozone (O_3), nitrogen dioxide (NO_2), formaldehyde (HCHO), and cloud fraction and cloud pressure. In addition, TEMPO spectra can also be used to derive sulfur dioxide (SO_2), bromine monoxide (BrO), glyoxal ($C_2H_2O_2$), water vapor (H_2O), nitrous acid (HNO_2), aerosols and Ultraviolet B (UVB) radiation. TEMPO thus can measure the major constituents, directly or by proxy, involved in tropospheric ozone (O_3) chemistry, as well as several other tropospheric and stratospheric constituents. TEMPO provides air quality products disseminated to the public via the Atmospheric Science Data Center (ASDC) at NASA LaRC.

TEMPO makes the first tropospheric trace gas measurements from geostationary orbit (GEO) for North America by building upon the heritage of six spectrometers operating in low Earth orbit (LEO): GOME (Burrows et al., 1999), SCIAMACHY (Bovensmann et al., 1999), OMI (Levelt et al., 2006), GOME-2 (Munro et al., 2016), OMPS (Flynn et al., 2014) and TROPOMI (Veefkind et al., 2012), as well as the GEMS instrument (Kim et al., 2020), launched into GEO in 2020 to measure air pollutants over eastern Asia. These legacy instruments have demonstrated the technologies necessary to provide the measurement precision required for TEMPO using very similar retrieval algorithms. Novel to the GEO missions are hourly measurements with finer spatial resolution. This observational strategy makes TEMPO an innovative application of well-proven techniques, producing a revolutionary dataset for air quality science and applications.

1.2. TEMPO Instrument and Measurements

Table 1 shows key characteristics of the TEMPO instrument and nominal hourly measurements. More instrument details can be found in Zoogman et al. (2017) and the TEMPO Level 1B Algorithm Theoretical Basis Document (Chong et al., 2025). The TEMPO instrument is a UV/visible imaging grating spectrometer using two 2-D 2k x 1k charge-coupled device (CCD) detectors in one focal plane covering the two bands ~293-494 nm (referred to as the UV band) and ~538-741 nm (VIS band). The 2k (2048) dimension is for the spatial direction and 1k (1028) dimension is for the spectral direction. The TEMPO instrument slit aligns with the North/South (N/S) direction and simultaneously measures 2048 (N/S or across-track) spatial pixels, of which 2036 pixels have good performance. Each band has 1028 spectral pixels, of which ~1016 pixels have good performance. The spectral resolution is ~0.6 nm at full width at half maximum (FWHM) and the spectral interval is ~0.2 nm.

Table 1. *TEMPO instrument and measurement characteristics*

Volume, Mass	1.4 m × 1.1 m × 1.2 m, 137 kg
Average operating power	138 W
Detector size	Two 2048 (spatial) × 1028 (spectral) detectors
Wavelength range	UV band: ~293 - 494 nm, Visible band: 538 - 741 nm
Spectral resolution	~0.6 nm @ FWHM (0.54-0.63 nm)
Spectral sampling	~0.2 nm or ~3 pixels / FWHM (2.7-3.2 nm)
Spectral co-registration[1]	< 0.1 pixel (for UV, visible, UV/visible)
Orbit	Geostationary (35786 km), 91.0°W above the Equator
Instantaneous field of view[2]	41.49 µrad (N/S) × 129.20 µrad (E/W)
Modulation Transfer Function @Nyquist[2]	0.31-0.41 (N/S) × 0.38-0.49 (E/W)
Field of view[2,3]	4.87° (N/S) × 8.66° (E/W)
Spatial resolution[2]	2.0 km (N/S) × 4.75 km (E/W) at center of field of regard (FOR) (33.5231° N, 89.2170° W)
Temporal resolution[4]	~1 hour, ~3-second snapshot per mirror step

Spectra per hour [2,3,4,5]	2036 (N/S) × 1181 (E/W)
Maximum Signal-to-Noise Ratio[6]	1372 – 1394 at 330 - 340 nm

[1]Smile (mapping of the same wavelength to different pixels of the focal plane for different spatial columns), keystone (deviation of signal mapping from the correct spatial channel across the focal plane), and UV/visible co-alignment are within 0.1 pixel.
[2]N/S represents the North/South (across-track) direction; E/W represents the East/West (mirror step) direction.
[3]Estimated with a 128 µrad E/W mirror step size (1.2 µrad overlapping between two steps) and 1181 positions.
[4]For the nominal mode. In the early morning or late afternoon, optimized modes can measure the daylight portion every ~40 minutes. Special modes can measure a selected portion of FOR every 5–10 minutes.
[5]2036 out of 2048 spatial pixels are valid pixels.
[6]For the nominal radiance without pixel binning, derived using in-flight data from September 1, 2023.

TEMPO can make three types of measurements: Earth-view radiance, solar irradiance, and dark current measurements. The Calibration Mechanism Assembly (CMA) controls the instrument aperture via a wheel with four selectable positions (open, closed, working diffuser, reference diffuser). The two diffusers allow recording of the top-of-atmosphere solar irradiance. The working diffuser is used on a more frequent (e.g., weekly) basis, and the reference diffuser is used every 3-6 months to assess trends in degradation of the working diffuser from radiation exposure and contamination. Solar measurements may be made when the Sun is unobscured within 30° to the instrument boresight during night. Earth-view radiance measurements are made in the open position during the daytime. Dark current data are collected with the wheel in the closed position a few times each day, before and after the Earth-view and before the solar measurements.

In a typical day, the TEMPO scan pattern includes optimized scanning in the early morning and late afternoon/evening, and nominal hourly scanning during the middle of the day. A TEMPO nominal hourly scan samples the entire field of regard (FOR) from East to West within 1 hour in 1181 mirror steps. The early morning and late afternoon/evening optimized scans increase the temporal sampling of the sunlit portion of the FOR to every 40 minutes by skipping observations over the dark parts of the continent. Observations of hourly scans are split into 9 granules; each granule includes ~6.7 minutes of data. Due to the fixed Instantaneous Field of View (IFOV), the footprint size on the ground depends on the viewing zenith angle (VZA). The footprint is ~2.0 x 4.75 km^2 at the center of the FOR, with an area varying from ~8 km^2 over Mexico City to ~21 km^2 over the Canadian oil sands. In addition to performing standard operations, TEMPO can use up to 25% of the observation time to perform special observations in high-time scan mode, scanning a selected portion of the FOR (i.e., N/S strip) at much higher temporal resolution (e.g., 5-10 minutes). Special observations can alternate with nominal hourly scans (e.g., 1-hour special observation followed by 1-hour nominal scan of FOR).

1.3. Nitrogen Dioxide

Figure 1 shows an example of tropospheric NO_2 retrievals from a typical hourly scan of TEMPO's field of regard. The data have been filtered for cloudy pixels as UV/visible measurements of tropospheric pollutants are generally not accurate in the presence of clouds. In this scan, enhanced levels of tropospheric NO_2 are clearly visible over many sources, including California's Central Valley, urban areas such as the San Francisco Bay Area, Phoenix and Toronto, and oil and gas producing regions like the Permian Basin.

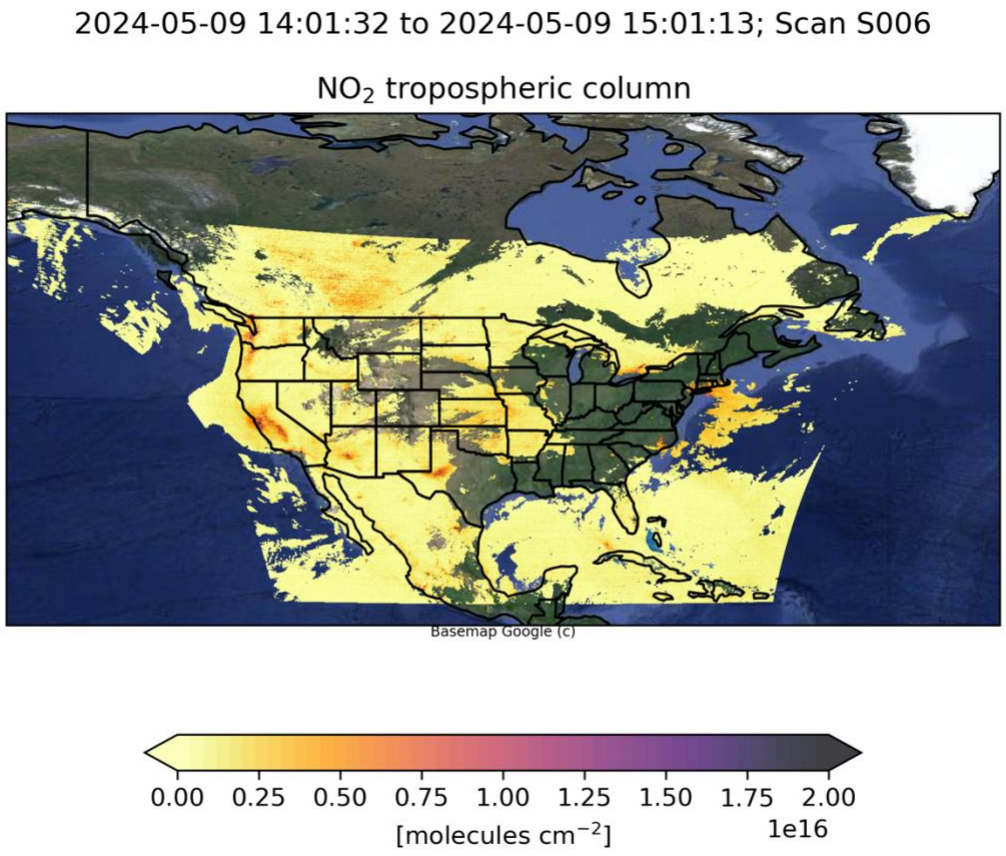

Figure 1. *NO_2 tropospheric vertical column densities retrieved using TEMPO spectra observed on May 9, 2024, scan 6. Due to large uncertainties in NO_2 retrievals over clouds, observations with radiative cloud fractions larger than 0.5 have been masked out to avoid misinterpretation.*

Nitrogen dioxide (NO_2) is a highly reactive gas that plays a critical role in air quality and tropospheric and stratospheric chemistry. NO_2 cycles rapidly with nitric oxide (NO) and these two molecules are collectively known as nitrogen oxides (NO_x = NO + NO_2). During daylight, this cycling happens on the scale of minutes, and measurements of NO_2 can be used as a proxy of total NO_x. NO_x reacts with volatile organic compounds (VOCs) in the presence of sunlight to form ozone. Near the ground, ozone can have significant detrimental effects on human health

and vegetation (U.S. EPA, 2020). Tropospheric ozone is additionally important through its role as a short-lived radiative forcer (IPCC, 2023b). NO_x is involved in the formation of secondary organic aerosols (SOAs), which are major contributors to premature mortality and morbidity from air pollution (Burnett et al., 2018) and which also impact radiative forcing (IPCC, 2023a). Its role in atmospheric chemistry means that NO_x influences the amount of the hydroxyl (OH) radical in the atmosphere (Fiore et al., 2024), with implications for the lifetimes of other species, including that of methane (Peng et al., 2022). NO_2 and other nitrogen-containing species contribute to the acidification and eutrophication of soils, water and vegetation through the addition of excess nitrogen by deposition, potentially resulting in a loss of biodiversity (Bobbink et al., 2010). Furthermore, NO_2 itself has direct detrimental effects on human health (U.S. EPA, 2016). As a result of these impacts, NO_x is designated as a criteria pollutant by the U.S. Environmental Protection Agency (EPA).

Tropospheric NO_x is emitted from the combustion of fossil fuels within transportation, power generation and industrial processes, as well as from lightning, microbial processes in soil, and biomass burning. NO_2 is removed from the atmosphere directly by dry deposition or by conversion to other nitrogen-containing species which are removed by either wet or dry deposition.

In the stratosphere, NO_2 is involved in ozone chemistry through reactions that destroy ozone and create hydrogen and chlorine reservoir species (Jacob, 2000). Most stratospheric NO_x results from the transport of the long-lived species nitrous oxide (N_2O) to the stratosphere, where N_2O has a lifetime of 116 ± 9 years (Prather et al., 2015). N_2O is produced by both anthropogenic (e.g., agriculture, fossil fuel combustion, sewage) and natural (biomass burning, soil and ocean nitrogen cycling) sources. Smaller stratospheric nitrogen sources include the dissociation of N_2 in the upper atmosphere, aircraft emissions, and lightning.

Nitrogen dioxide has strong spectral absorption features in the visible and near-UV region of the electromagnetic spectrum which permit the measurement of NO_2 from satellite remote sensing instruments viewing backscattered solar light. This ATBD describes the retrieval algorithm developed by the Smithsonian Astrophysical Observatory (SAO) to generate NO_2 trace gas products from TEMPO observations.

1.4. Nitrogen Dioxide Measurements from Space

TEMPO evolved from the 2007 Earth Science Decadal Survey (National Research Council, 2007) GEO-CAPE mission (Fishman et al., 2012) for atmospheric chemistry and ocean color measurements from geostationary orbit, which recommended measurements of O_3, NO_2, SO_2, HCHO, $C_2H_2O_2$ and aerosols from an ultraviolet/visible (UV/Vis) component. TEMPO was designed to achieve as much as possible of the GEO-CAPE atmospheric UV/Vis measurement capability within the cost constraints of the NASA Earth Venture Program.

TEMPO benefits from the heritage of a long history of sensors flown in low Earth orbit (LEO) (González Abad et al., 2019). The first nadir-backscatter NO_2 observations were made from space with the GOME instrument (Burrows et al., 1999), which launched on the ERS-2 satellite in 1995. Multi-year NO_2 retrievals have since been produced with observations from LEO using GOME (Martin et al., 2002; Richter & Burrows, 2002) (ERS-2 satellite; 1995-2011), SCIAMACHY (Boersma et al., 2008) (Envisat; 2002-2012), OMI (Boersma et al., 2011; Bucsela et al., 2013; Lamsal et al., 2021) (Aura; 2004-present), GOME-2 (S. Liu et al., 2019; Richter et al., 2011) (Metop-A/Metop-B/Metop-C; 2006-2021/2012-present/2018-present), OMPS (Huang et al., 2022; Yang et al., 2014) (Suomi-NPP/NOAA-20; 2012-present/2017-present), TROPOMI (van Geffen, Eskes, Compernolle, et al., 2022) (Sentinel-5P; 2017-present), and EMI (Zhang et al., 2020) (GaoFen-5; 2018-present). Additionally, recent efforts have been made to create long-term consistent data records of NO_2 from multiple LEO instruments, including through the European Quality Assurance for Essential Climate Variables (QA4ECV) (Boersma et al., 2018; Zara et al., 2018) and Climate Change Initiative (CCI) programs, and the NASA Multi-Decadal Nitrogen Dioxide and Derived Products from Satellites (MINDS) project.

NO_2 measurements from geostationary orbit are now performed daily by the GEMS instrument (Kim et al., 2020) (GEO-KOMPSAT-2B; 2020-present) over Asia. The Sentinel-4/UVN instrument is expected to launch into geostationary orbit in 2025, from where it will make NO_2 measurements over Europe and North Africa. Together, GEMS, TEMPO and Sentinel-4/UVN form the first constellation of air quality sensors capable of measuring NO_2 from geostationary orbit.

2. Context/Background

2.1. Historical Perspective

2.1.1. Algorithm Heritage

The TEMPO NO_2 retrieval algorithm has its heritage in the trace gas retrieval algorithms used by the SAO to produce the OMI operational data products OMHCHO (HCHO) (González Abad et al., 2015), OMBRO (BrO) (Suleiman et al., 2019) and OMOCLO (OClO). These algorithms are also used to produce the OMI research products glyoxal (Chan Miller et al., 2014; Kwon et al., 2024) and water vapor (Wang et al., 2019). The OMI algorithms are derived from algorithms originally developed for GOME (Chance et al., 2000; Martin et al., 2002). In addition to OMI, these algorithms have been applied to retrieve a range of trace gases from several other satellite (González Abad et al., 2016; Nowlan et al., 2011, 2023; Parrella et al., 2013; Sioris et al., 2004) and airborne (C. Liu et al., 2015; Nowlan et al., 2016, 2018) instruments. In addition to its heritage in SAO retrieval algorithms, the TEMPO NO_2 retrieval algorithm has heritage in NASA GSFC's operational NO_2 product OMNO2 (Lamsal et al., 2021) through the TEMPO O_2-O_2 cloud algorithm (Wang et al., 2025) and the application of geometry-dependent surface Lambert equivalent reflectivity (GLER) (Fasnacht et al., 2019; Qin et al., 2019).

During the development of the SAO Science Data Processing Center (SDPC) operational pipeline, a modified version of the operational SAO OMI trace gas algorithm (González Abad et al., 2015) was implemented for the processing of TEMPO trace gases with multiple updates as described in this ATBD. The NO_2 and HCHO baseline trace gas products share the same retrieval algorithm. They differ in the use of either a solar irradiance (NO_2) or a radiance reference (HCHO) for the spectral fitting reference spectrum and diverge in a final processing step where NO_2 is separated into its tropospheric and stratosphere components, and the HCHO column is corrected for the use of a background reference spectrum.

2.1.2. Algorithm Overview and Implementation

TEMPO data products are generated by the SDPC at the Smithsonian Astrophysical Observatory and then pushed to the NASA Atmospheric Science Data Center for public distribution. These products include Level 1B spectra (calibrated solar irradiance and geolocated Earth-view radiances), Level 2 trace gas and cloud products (at the native ground pixel footprint for the East-West granules that make up a TEMPO scan) and Level 3 trace gas and cloud products (Level 2 data sampled on a regular grid for all granules constituting a single East-West scan).

The SDPC generates the TEMPO products in the following order from Level 0 (raw data): 1) Level 1B; 2) Level 2 clouds; 3) Level 2 trace gases; and 4) Level 3 products. This order is required because the trace gas products are derived from the Level 1B spectra, and also require the cloud fraction and pressure for the derivation of air mass factors used in their vertical column density calculations.

2.1.3. Product Version

This document describes the TEMPO version 3 NO_2 product produced through the SDPC operational processing pipeline. The version 3 product was initially released to the public on May 20, 2024. Updates to the TEMPO operational pipeline result in periodic new data releases. The TEMPO trace gas and cloud user guide (González Abad et al., 2024) provides additional information on versioning history, data format and usage recommendations. Table 2 describes the major public data releases and algorithm updates.

Table 2. *Product and Science Data Processing Center pipeline versions for public data releases*

Product Version Designation	**Science Data Processing Center Pipeline Version**	**Release Date**	**Significant Algorithm Updates**
V03	4.4	May 20, 2024	First major public release

2.2. Additional Information

Table 3. *List of acronyms and abbreviations*

Acronym/Abbreviation	Definition
AEROMMA	Atmospheric Emissions and Reactions Observed from Megacities to Marine Areas
AMF	Air mass factor
AQS	Air Quality System
ASDC	Atmospheric Science Data Center
ATBD	Algorithm theoretical basis document
BRDF	Bidirectional Reflectance Distribution Function
CCD	Charge-coupled device
CCI	Climate Change Initiative
CMA	Calibration Mechanism Assembly
CMAQ	Community Multiscale Air Quality
CUPiDS	Coastal Urban Plume Dynamics Study
DEM	Digital elevation model
DU	Dobson Unit
E/W	East/West
EMI	Environment Monitoring Instrument
EPA	Environmental Protection Agency
ERS-2	European Remote-Sensing Satellite-2
EVI	Earth Venture Instrument
FOR	Field of regard
FWHM	Full width at half maximum
GEMS	Geostationary Environment Monitoring Spectrometer
GEO	Geostationary orbit
GEO-CAPE	Geostationary Coastal and Air Pollution Events
GEOS	Goddard Earth Observing System
GEOS-CF	GEOS Composition Forecast
GEOS FP-IT	GEOS Forward Processing Instrument Teams
GLER	Geometry-dependent surface Lambert equivalent reflectivity
GMAO	Global Modeling and Assimilation Office
GMTED2010	Global Multi-resolution Terrain Elevation Data 2010
GOME	Global Ozone Monitoring Experiment
GSFC	Goddard Space Flight Center
HEMCO	Harmonized Emissions Component
HAMAP	Hemispheric Airborne Measurements of Air Quality
HTAP	Hemispheric Transport of Air Pollution

IFOV	Instantaneous Field of View
IMS	Interactive Multisensor Snow and Ice Mapping System
INR	Image Navigation and Registration
IS	Intelsat
LaRC	Langley Research Center
LEO	Low Earth orbit
LUT	Look-up table
MAX-DOAS	Multi-AXis Differential Optical Absorption Spectroscopy
MEGAN	Model of Emissions of Gases and Aerosols from Nature
MINDS	Multi-Decadal Nitrogen Dioxide and Derived Products from Satellites
MODIS	Moderate Resolution Imaging Spectroradiometer
N/S	North/South
NASA	National Aeronautics and Space Administration
NDACC	Network for the Detection of Atmospheric Composition Change
NEC-AQ-GHG	NorthEast Corridor Air Quality and Greenhouse Gas
NOAA	National Oceanic and Atmospheric Administration
OMBRO	OMI bromine monoxide level 2 product
OMHCHO	OMI formaldehyde level 2 product
OMI	Ozone Monitoring Instrument
OMNO2	OMI nitrogen dioxide level 2 product
OMOCLO	OMI chlorine dioxide level 2 product
OMPS	Ozone Mapping and Profiler Suite
PGN	Pandonia Global Network
PI	Principal Investigator
PLRA	Program Level Requirements Appendix
PROFOZ	OMI ozone profile level 2 product
QA4ECV	Quality Assurance for Essential Climate Variables
QFED	Quick Fire Emission Database
RETRO	REanalysis of the TROpospheric chemical composition
SAO	Smithsonian Astrophysical Observatory
SARP	Student Airborne Research Program
SCD	Slant column density
SCIAMACHY	SCanning Imaging Absorption spectroMeter for Atmospheric CHartographY
SDPC	Science Data Processing Center
SOA	Secondary organic aerosol
SNR	Signal-to-noise ratio
STAQS	Synergistic TEMPO Air Quality Science

Suomi NPP	Suomi National Polar-orbiting Partnership
SZA	Solar zenith angle
TEMPO	Tropospheric Emissions: Monitoring of Pollution
TOA	Top of atmosphere
TROPOMI	TROPOspheric Monitoring Instrument
US	United States
USGS	United States Geological Survey
UV	Ultraviolet
UVB	Ultraviolet B
VCD	Vertical column density
VLIDORT	Vector LInearized Discrete Ordinate Radiative Transfer
VOC	Volatile organic compound
VZA	Viewing zenith angle
WRF-Chem	Weather Research and Forecasting - Chemistry

Table 4. *List of symbols used in mathematical equations*

Meaning	**Symbol**
Albedo	α
Albedo (cloud)	α_c
Albedo (snow)	α_s
Albedo (snow free surface)	α_f
Altitude	z
Air mass factor	AMF
Cloud fraction (effective)	f_{ce}
Cloud fraction (radiative)	f_{cr}
Cloud pressure	p_c
Covariance matrix of measurement errors	$\mathbf{S}_\epsilon$
Earth's surface gravity acceleration	g
Gas constant of dry air	R
Gas partial column	n

Geometric air mass factor	AMF_{geo}
Hybrid sigma-pressure vertical grid: first Eta coefficient	eta_a
Hybrid sigma-pressure vertical grid: second Eta coefficient	eta_b
Look-up table variables for radiances and scattering weights	I_0, I_1, I_2, I_r, S_b
Model parameters spectral fit	$\mathbf{b}$
Modeled radiance spectrum	$\mathbf{F}$
Observed radiance spectrum	$\mathbf{y}$
Profile shape factor	S
Relative azimuth angle	ϕ
Retrieval state vector for spectral fit	$\mathbf{x}$
Scattering weight	W
Scattering weight: clear sky	W_{clear}
Scattering weight: cloudy sky	W_{cloud}
Slant column density	SCD
Snow/ice fraction	f_s
Solar irradiance	I_0
Solar zenith angle	θ_0
Stratosphere-troposphere separation boxcar filter parameters	w, A, B, N
Stratospheric air mass factor	AMF_{strat}
Stratospheric slant column density	SCD_{strat}
Stratospheric vertical column density	VCD_{strat}
Super-Gaussian asymmetry parameter	a_q
Super-Gaussian exponent (shape) parameter	k
Super-Gaussian instrument line shape function	s
Super-Gaussian instrument line shape normalization factor	A_s

Super-Gaussian width parameter	q
Surface pressure	p_s
Surface temperature	T_s
Temperature	T
Temperature of reference cross section	T_σ
Temperature correction factor	c
Temperature lapse rate	Γ
Terrain altitude	h
TOA radiance	I
TOA radiance (clear sky)	I_{clear}
TOA radiance (cloudy sky)	I_{cloud}
Total air mass factor (surface to top of atmosphere)	AMF_{total}
Total vertical column density (surface to top of atmosphere)	VCD_{total}
Tropospheric air mass factor	AMF_{trop}
Tropospheric slant column density	SCD_{trop}
Tropospheric vertical column density	VCD_{trop}
Vertical column density	VCD
Viewing zenith angle	θ
Wavelength	λ

Table 5. *List of chemical formulas*

Meaning	**Formula**
Bromine monoxide	BrO
Chlorine dioxide	$OClO$
Formaldehyde	$HCHO$
Glyoxal	$C_2H_2O_2$
Hydroxyl	OH
Iodine Oxide	IO
Nitric oxide	NO
Nitric oxide + nitrogen dioxide	NO_x
Nitrogen dioxide	NO_2
Nitrous acid	HNO_2
Nitrous oxide	N_2O
Molecular oxygen	O_2
Molecular oxygen collision complex	O_2-O_2
Ozone	O_3
Sulfur dioxide	SO_2
Water vapor	H_2O

3. Algorithm Description

3.1. Scientific Theory

3.1.1. Overview

The TEMPO retrieval algorithm used to produce Level 2 NO_2 tropospheric, stratospheric and total vertical column densities has three major processing steps:

1. Spectral fitting to calculate slant column densities (SCDs);

2. Tropospheric and stratospheric air mass factor (AMF) calculations for converting SCDs to vertical column densities (VCDs); and
3. Separation of the stratospheric and tropospheric VCDs.

Figure 2 summarizes the major inputs, outputs and processing steps that will be described in this section.

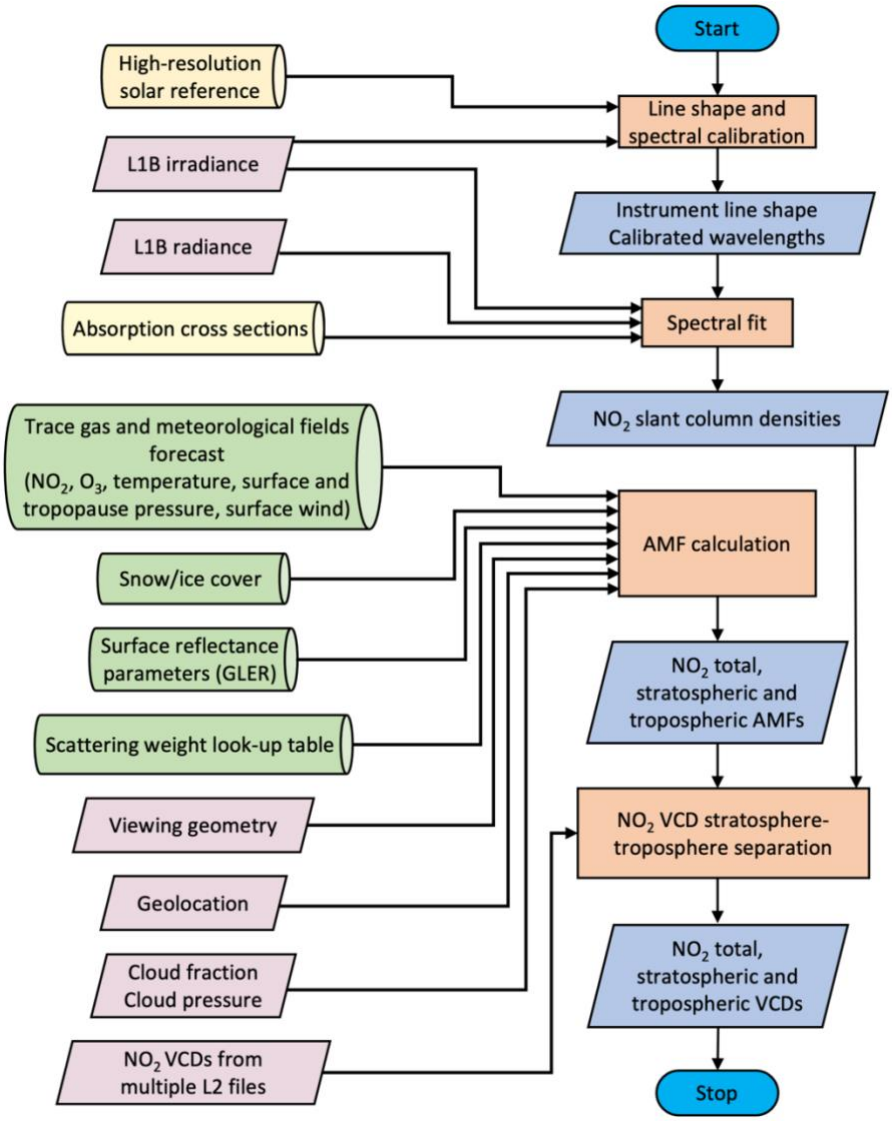

Figure 2. *Flow chart of TEMPO NO_2 retrieval algorithm, showing slant column fitting input databases (yellow cylinders), AMF input databases (green cylinders), variable inputs from TEMPO Level 1B spectra and cloud information (pink parallelograms), algorithm input/outputs (blue parallelograms) and major processes (orange rectangles).*

The TEMPO Level 2 NO_2 product includes tropospheric, stratospheric and total NO_2 VCDs.

The total vertical column density (VCD_{total}) of NO_2 is related to the slant column density of the gas observed by the instrument by

$$VCD_{total} = \frac{SCD}{AMF_{total}} \quad (1)$$

where AMF_{total} is the air mass factor determined for the mean path of sunlight as it travels through the atmosphere before its detection by TEMPO.

The tropospheric vertical column density (VCD_{trop}) of NO_2 is related to the slant column density by

$$VCD_{trop} = \frac{(SCD - VCD_{strat} \cdot AMF_{strat})}{AMF_{trop}} \quad (2)$$

where AMF_{strat} and AMF_{trop} represent the stratospheric and tropospheric air mass factors and VCD_{strat} represents the stratospheric column calculated in the stratosphere-troposphere separation step as described below.

Note that the use of the NO_2 VCD_{total} provided as supporting data in the product is discouraged for most users. Instead, users who wish to use the total column should use the sum of the tropospheric and stratospheric VCD. (Section 4.2 for more details.)

3.1.2. Slant Column Density Retrieval

3.1.2.1. Theoretical Basis for Spectral Fitting

Slant columns are derived using least-squares minimization to directly fit a modeled radiance spectrum **F(x, b)** to an observed radiance spectrum **y** through non-linear least-squares Levenberg-Marquart minimization of a cost function χ^2:

$$\chi^2 = [\boldsymbol{y} - \boldsymbol{F}(\boldsymbol{x}, \boldsymbol{b})]^T \boldsymbol{S}_{\epsilon}^{-1} [\boldsymbol{y} - \boldsymbol{F}(\boldsymbol{x}, \boldsymbol{b})] \quad (3)$$

where $\mathbf{S}_{\varepsilon}$ is the covariance matrix of measurement errors. In practice, errors on individual detector pixels in the detector array are assumed to be uncorrelated, and $\mathbf{S}_{\varepsilon}$ is included as a diagonal matrix.

The modeled spectrum is a function of pre-determined model parameters **b** and the retrieved state vector **x**. The modeled spectrum at each wavelength λ is represented by

$$F(\lambda) = [x_a I_0(\lambda) + b_u(\lambda)x_u + b_r(\lambda)x_r]e^{-\sum_i b_i(\lambda)x_i} \sum_j \left(\lambda - \bar{\lambda}\right)^j x_j^{SC} + \sum_k \left(\lambda - \bar{\lambda}\right)^k x_k^{BL}. \quad (4)$$

In this equation, I_0 is the solar irradiance observed by TEMPO scaled by a retrieved intensity parameter x_a (which mainly represents reflectance off the surface or clouds). The solar irradiance I_0 is observed by directly viewing the Sun once a week through a diffuser.

The term $b_u(\lambda)$ describes a correction for spectral undersampling (Chance et al., 2005), while $b_r(\lambda)$ represents the effects of rotational Raman (Ring) scattering (Chance & Spurr, 1997). The retrieved slant columns for the trace gas of interest (NO_2) and any other spectrally interfering gases are represented by x_i. Their absorption cross sections, convolved with the instrument line shape and corrected for the "I_0 effect" (Aliwell et al., 2002), are included as $b_i(\lambda)$. The "I_0 effect" accounts for the influence of absorption features in the solar spectrum on the retrieval of absorbing trace gases. In addition, the retrieval also determines scaling (of order j) and baseline (of order k) polynomial coefficients (x^{SC} and x^{BL}) that represent low frequency wavelength-dependent effects from surface reflectivity, molecular scattering, aerosols and instrument artifacts.

3.1.2.2. Spectral Calibration Using On-Orbit Data

Prior to the main spectral fitting, the TEMPO instrument line shape is derived and the detector-pixel-to-wavelength spectral calibration is refined by fitting the Level 1B irradiance spectrum to a simulated solar spectrum. The simulated solar spectrum is calculated by convolving a high-resolution solar reference spectrum with the instrument line shape. This step follows a calibration approach used in previous SAO trace gas retrievals (Bak et al., 2017; Sun et al., 2017). The algorithm simultaneously retrieves the wavelength registration (using a constant shift from the first-guess wavelengths provided in the Level 1B irradiance) and three terms (width factor q, shape factor k and asymmetry factor a_q) that define the instrument line shape represented by a super-Gaussian (Beirle et al., 2017)

$$s(\Delta\lambda) = A_s \cdot exp\left[-\left|\frac{\Delta\lambda}{q + \mathrm{sgn}(\Delta\lambda)a_q}\right|^k\right], \quad (5)$$

where $\Delta\lambda$ is the wavelength distance from the center of the instrument line shape function, sgn() is the sign function used to define the two sides of the instrument line shape, and A_s is a normalization factor. We determine an instrument line shape function for each across-track position of the CCD array using the entire NO_2 wavelength fitting window. The line shape parameters are saved for each across-track position and later applied to all retrievals at that position. Figure 3 shows the results of the spectral calibration in the NO_2 fitting window (405 - 465 nm) of the solar irradiance reference used to retrieve NO_2 from scan 6 on May 9, 2024.

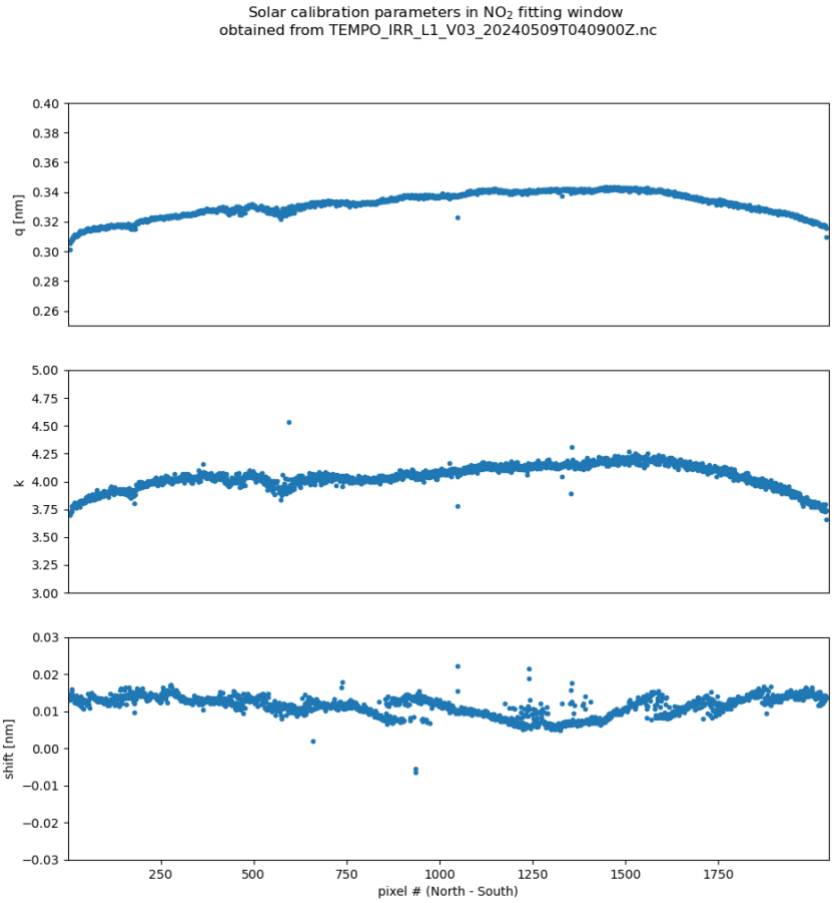

Figure 3. *Spectral calibration results showing half-width of the slit function at 1/e of the slit function's peak (top panel), shape factor (middle) and the wavelength grid shift (bottom) as a function of across-track detector pixel index (ordered North to South). As the TEMPO slit functions in the NO_2 spectral fitting window show high symmetry, the spectral calibration algorithm uses a fixed asymmetry factor of $a_q = 0$.*

3.1.2.3. Application to NO_2

The TEMPO NO_2 slant column density retrieval uses the fitting window 405 - 465 nm. Table 6 describes the fitting details used for the TEMPO retrievals. The retrieval simultaneously fits slant column densities (x_i) for nitrogen dioxide (NO_2), ozone (O_3), the oxygen collision pair (O_2-O_2) and water vapor (H_2O), absorption by liquid H_2O, the Ring spectrum magnitude (x_r), closure scaling (x^{SC}) polynomials and baseline (x^{BL}) polynomials that account for low-frequency effects (such as Rayleigh and Mie scattering), a correction for undersampling (x_u), and a wavelength shift which represents the difference in detector pixel wavelength registration between the backscattered radiance spectrum and the solar irradiance reference spectrum. This shift in

wavelength calibration is typically due to thermal changes in the instrument over the course of a day, as well as inhomogeneous scene illumination (Noël et al., 2012; Voors et al., 2006). Figure 4 shows an example of the cross sections and the molecular Ring spectrum used in the retrieval of the NO_2 SCD. Figure 5 shows the retrieved NO_2 SCD for scan 6 on May 9, 2024.

Table 6. *Parameters fit in TEMPO NO_2 slant column density retrieval*

Parameter	**Details**
NO_2	Vandaele et al. (1998), 220 K
O_3	Serdyuchenko et al. (2014), 223 K
O_2-O_2	Finkenzeller & Volkamer (2022), 293 K
H_2O	Gordon et al. (2022), 283 K and 912 hPa
Liquid H_2O	Mason et al. (2016)
Undersampling	Chance et al. (2005)
Molecular Ring effect	Chance & Spurr (1997)
Scaling polynomial	4th order
Baseline polynomial	4th order
Wavelength shift	Single value for the entire fitting window

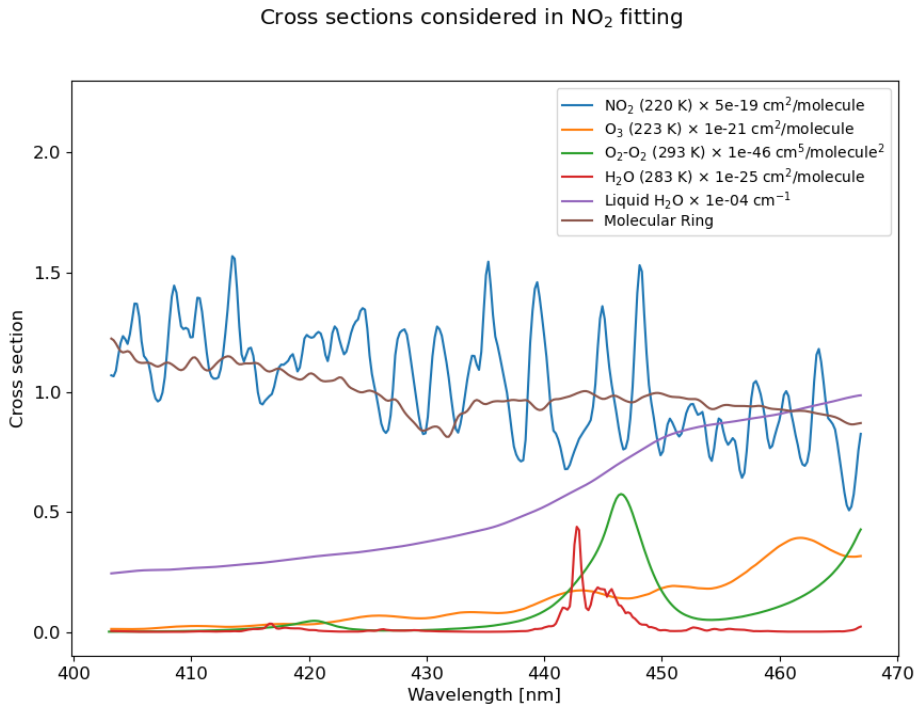

Figure 4. *Absorption cross sections and molecular Ring spectrum considered in the TEMPO retrievals of NO_2, convolved with the TEMPO instrument line shape function at across-track (N/S) position 1000 on October 6, 2023.*

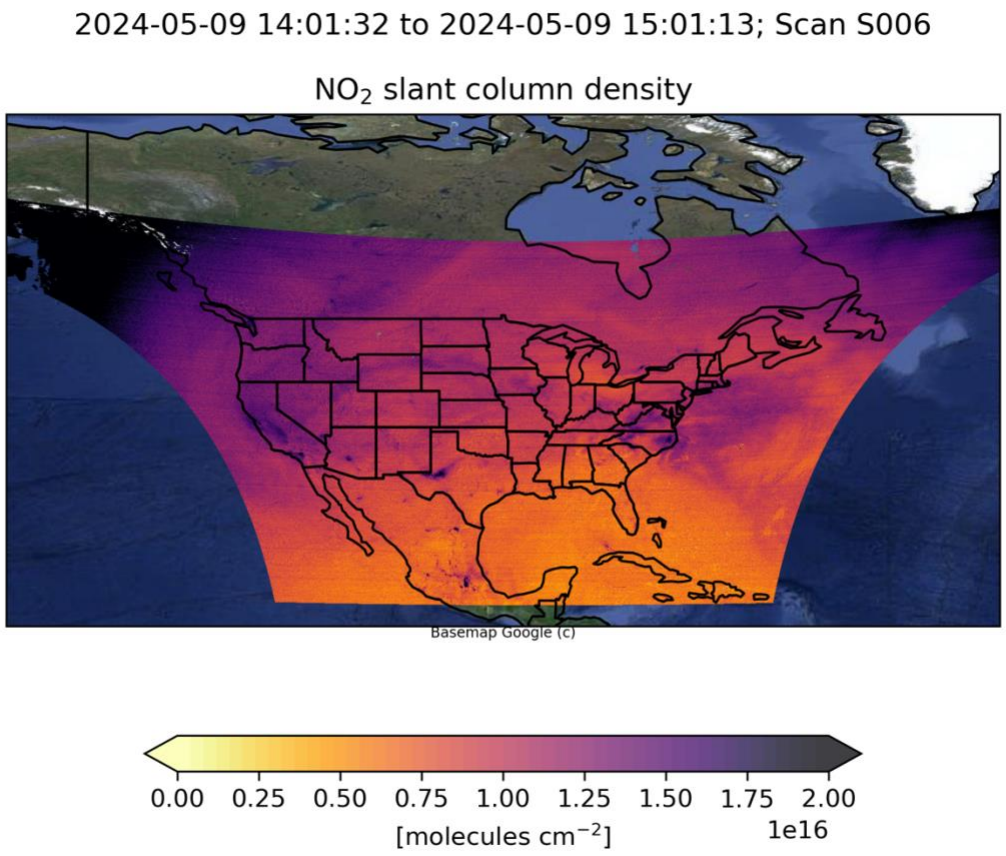

Figure 5. *Retrieved NO_2 slant column density for scan 6 on May 9, 2024.*

3.1.2.4. Treatment of Bad Detector Pixels

The spectral fitting code excludes detector pixels that are flagged in the Level 1B variable *pixel_quality_flag* as "missing_data", "bad_pixel", "processing_error", or "saturated", by de-weighting the detector pixel in the fit. The Level 1B ATBD (Chong et al., 2025) provides further detail regarding the methodology used to determine the value of the *pixel_quality_flag* in the Level 1B files.

The TEMPO retrieval also employs a "hot pixel" spike removal procedure, which removes the effect of anomalous detector radiance spikes. After spectral fitting, any TEMPO detector pixels that shows greater than a given σ deviation (3 times the standard deviation in the case of NO_2) from the mean fitting residual are flagged, and the spectral fitting is repeated excluding those pixels. For LEO instruments, these hot pixels primarily occur due to energetic particles that may impact detectors as satellites pass through the region affected by the South Atlantic Anomaly.

Given the novel GEO orbit of TEMPO, it is an unknown how often these "hot" pixels will appear. Initial analysis suggests a small impact on the retrieval results.

3.1.3. Air Mass Factor Calculation

3.1.3.1. Overview

The air mass factors are calculated on a scene-by-scene basis using the formulation of Palmer et al. (2001) and Martin et al. (2002), for an assumed atmosphere with optically thin absorbers. The photon path is assumed to be constant within the wavelength fitting window, and for NO_2 the AMF is determined at 440 nm. The AMF is defined as a function of altitude-dependent scattering weights *W(z)* and a profile shape factor *S(z)*.

The tropospheric air mass factor AMF_{trop} is determined using the scattering weights and profile shape from the surface to the tropopause and is defined as

$$AMF_{trop} = \int_{surface}^{tropopause} W(z)S(z)c(z)dz, \quad (6)$$

where *c(z)* is an altitude-dependent temperature correction factor. The temperature correction is required because NO_2 spectral absorption is temperature-dependent, but the retrieval is performed using a single cross section at 220 K. This correction is discussed in more detail in Section 3.1.3.7.

Similarly, the stratospheric air mass factor AMF_{strat} is determined using the scattering weights and profile shape from the tropopause to the top of the atmosphere (TOA) and is defined as

$$AMF_{strat} = \int_{tropopause}^{TOA} W(z)S(z)c(z)dz. \quad (7)$$

The AMF of the total column is defined as

$$AMF_{total} = \int_{surface}^{TOA} W(z)S(z)c(z)dz. \quad (8)$$

The profile shape factor is the NO_2 profile normalized over the altitude range of interest. It is calculated from the partial columns of the trace gas in each layer, *n(z)*, using

$$S(z) = \frac{n(z)}{\int_z n(z)dz}. \quad (9)$$

In the case of operational TEMPO processing, these partial columns are determined from the GEOS-CF chemical transport model which is described in a later section.

Figure 6 shows the AMFs calculated for the tropospheric, stratospheric and total NO_2 columns for scan 6 on May 9, 2024. The following sections describe the different inputs used in the calculation of the AMFs.

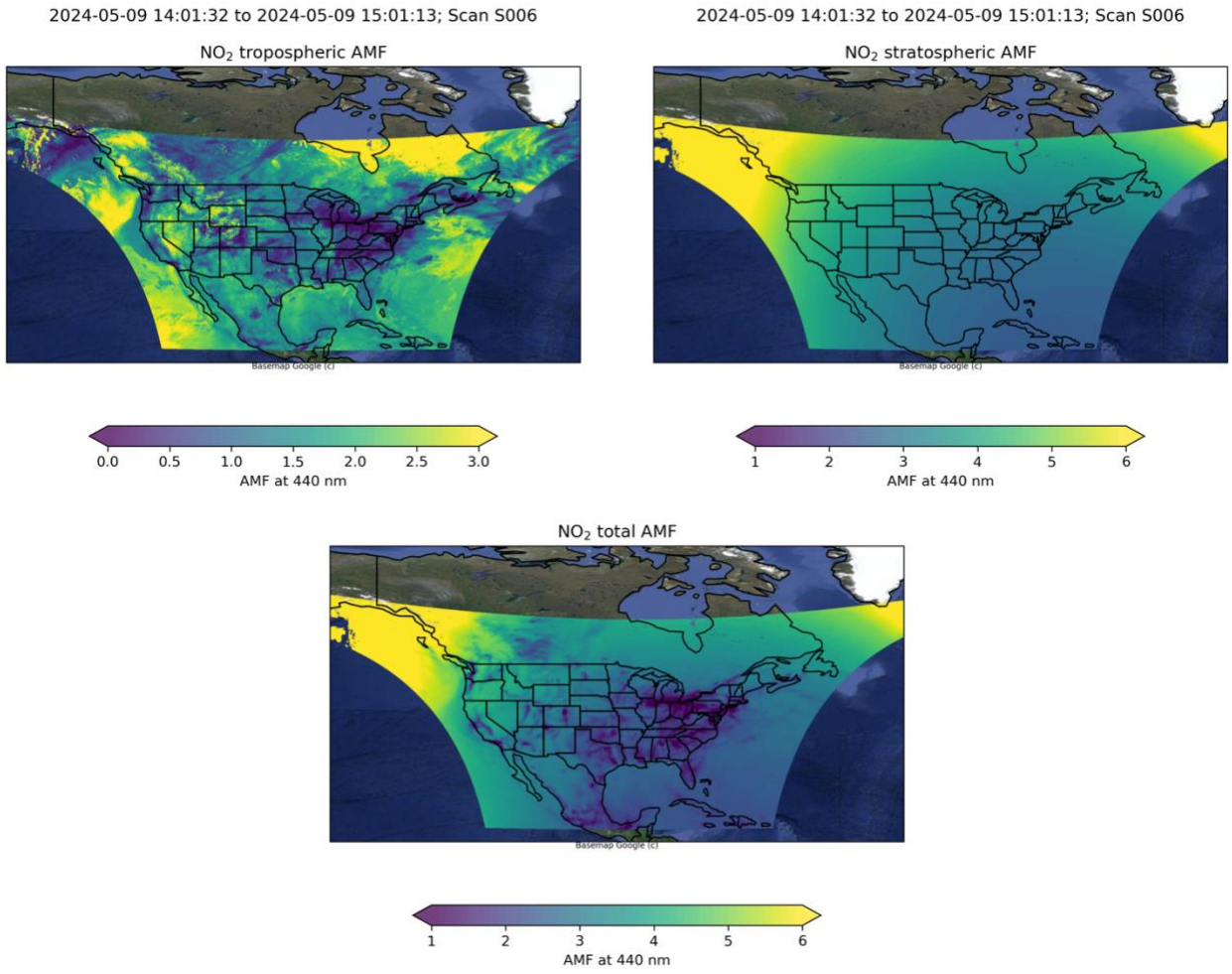

Figure 6. *NO_2 tropospheric, stratospheric and total AMFs calculated for TEMPO scan 6 on May 9, 2024. The stratospheric AMF is primarily determined by viewing geometry, while the tropospheric and total AMFs show larger heterogeneity from the contributions of cloud cover, surface reflectance, and NO_2 trace gas profile shape.*

3.1.3.2. Radiative Transfer Model and Look up Tables

The scattering weights *W(z)* describe the sensitivity of the NO_2 retrieval at different altitudes. *W(z)* and TOA radiances depend on wavelength, viewing geometry, atmospheric scattering (both

Rayleigh molecular scattering and Mie scattering associated with clouds and aerosols) and surface properties. Owing to the computational cost of simulating scattering weights and TOA radiances using radiative transfer models, it is common to use pre-computed look up tables (LUTs). In the case of TEMPO NO_2, the algorithm uses an LUT calculated with version 2.8 of the Vector LInearized Discrete Ordinate Radiative Transfer (VLIDORT) model (Spurr, 2006). The LUT provides information on *W(z)* and TOA radiances for clear (I_{clear}) and cloudy (I_{cloud}) observations as a function of altitude (z) (expressed as atmospheric pressure), solar zenith angle (θ_0), viewing zenith angle (θ), surface albedo (α), surface pressure (p_s), cloud pressure (p_c) and representative ozone profile. Aerosols are not explicitly treated in the retrieval. Table 7 summarizes the nodes of the LUT.

The 22 ozone profiles employed in the VLIDORT simulations were derived using OMI ozone profile retrievals (PROFOZ) (X. Liu et al., 2010). These profiles represent climatological values for three latitudinal bands: |latitude| < 30° for the tropical band (L), 30°< |latitude| < 60° for the middle latitude band (M) and |latitude| > 60° for the polar latitude band (H). For each latitudinal band several representative ozone total columns were computed. The specific nodes for the LUT interpolation are selected based on the observation latitude and an ozone column derived from the a priori ozone profile (see Section 3.1.3.5 for more detail on atmospheric profile inputs).

To improve computing efficiency, the LUT stores the variables I_0, I_1, I_2, I_r, S_b, dI_0, dI_1 and dI_2 from which linear interpolation can be applied to recover the TOA radiance (I) and scattering weights *W(z)* using the relative azimuth angle ϕ and albedo α with the following expressions:

$$I = I_0 + I_1 \cdot cos(\phi) + I_2 \cdot cos(2\phi) + \frac{I_r \cdot \alpha}{(1 - \alpha \cdot S_b)} \quad (10)$$

and

$$W(z) = dI_0 + dI_1 \cdot cos(\phi) + dI_2 \cdot cos(2\phi). \quad (11)$$

The first three terms of the radiance equation describe the atmospheric component of the radiance, with I_0, I_1 and I_2 being dependent on the solar and viewing zenith angles. The last term in the equation provides the surface contribution, where $Ir \cdot \alpha$ is the direct reflection from a Lambertian surface with albedo α and $(1 - \alpha \cdot S_b)^{-1}$ represents multiple reflections between the surface and the atmosphere.

Since ozone absorption is not very strong in the NO_2 fitting window for solar zenith angles smaller than 70°, the wavelength dependency of *W(z)* is small. In consequence, only one LUT derived at 440 nm is used. For solar zenith angles larger than 70° the assumption of an optically thin atmosphere starts to break down and the derivation of AMFs as described here loses accuracy.

Table 7. *Nodes for TEMPO NO_2 look-up table. The last three digits of the ozone profile identifiers indicate the total column in Dobson Units (DU). For example, L200 indicates the 200 DU tropical latitude profile.*

Parameter	Number of nodes	Nodes
Solar zenith angle (θ_0) [degree]	11	0, 15, 30, 45, 55, 65, 70, 75, 80, 85, 89.9
Viewing zenith angle (θ) [degree]	11	0, 15, 30, 45, 55, 65, 70, 75, 80, 85, 89.9
Surface albedo (α)	8	0.0, 0.01, 0.05, 0.1, 0.2, 0.5, 0.8, 1.0
Surface or cloud pressure (p_s/p_c) [hPa]	12	50, 100, 200, 300, 400, 500, 600, 700, 800, 900, 1013, 1050
Ozone profile	22	Tropical latitudes: L200, L250, L300, L350 Middle latitudes: M200, M250, M300, M350, M400, M450, M500, M550 Polar latitudes: H100, H150, H200, H250, H300, H350, H400, H450, H500, H550
Pressure levels [hPa]	47	0, 0.1, 0.2, 0.5, 0.9, 1.3, 2.0, 2.9, 4.4, 6.7, 10.3, 16.0, 25.2, 40.2, 64.6, 100.0, 150.0, 200.0, 250.0, 300.0, 350.0, 400.0, 425.0, 450.0, 475.0, 500.0, 525.0, 550.0, 575.0. 600.0, 625.0, 650.0, 675.0, 700.0, 725.0, 750.0, 775.0, 800.0, 825.0, 850.0, 875.0, 900.0, 925.0, 950.0, 975.0, 1013.0, 1050.0

Figure 7 shows typical scattering weights for clear and cloudy sky observations derived from the LUT tables, as well as sample NO_2 profiles used to determine shape factors (see Section 3.1.3.5 for information on the GEOS-CF gas profiles).

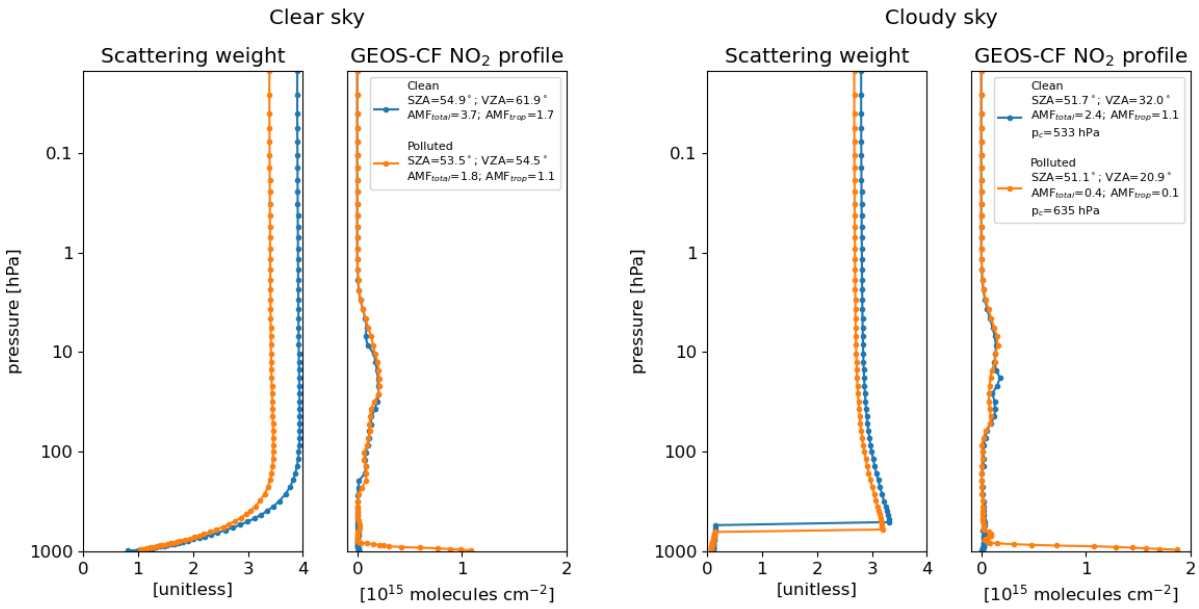

Figure 7. *Sample scattering weights for clear-sky (cloud-free) and cloudy observations, as well as vertical profiles of NO_2 partial columns in clean and polluted areas forecasted by GEOS-CF and used in the calculation of AMFs for four ground pixels in TEMPO's granule 5, scan 6 on May 9, 2024. Under polluted conditions (orange lines), the GEOS-CF gas profiles have greatly increased partial columns in the boundary layer relative to clean conditions (blue lines). The cloudy sky scattering weights (right half of the figure) show greatly reduced sensitivity below the cloud relative to clear sky conditions (left half of the figure).*

3.1.3.3. Clouds

The AMF for a partly cloudy scene is determined using the independent pixel approximation (Martin et al., 2002). In this case the scattering weight for the pixel is determined using

$$W(z) = (1 - f_{cr}) \cdot W_{clear}(z, \alpha, p_s) + f_{cr} \cdot W_{cloud}(z, \alpha_c, p_c) \quad (12)$$

where $W_{clear}(z, \alpha, p_s)$ is the scattering weight associated with a fully cloud-free scene at a particular altitude (z) for a given viewing geometry with surface albedo (α) and surface pressure (p_s), and $W_{cloud}(z, \alpha_c, p_c)$ is the scattering weight associated with a hypothetical fully cloudy scene. Clouds are considered in the radiative transfer simulation as Lambertian surfaces with an albedo (α_c) of 0.8 placed at the cloud pressure height (p_c). The cloud radiance fraction f_{cr} is defined as

$$f_{cr} = \frac{f_{ce} \cdot I_{cloud}}{(1 - f_{ce}) \cdot I_{clear} + f_{ce} \cdot I_{cloud}} \quad (13)$$

where I_{clear} and I_{cloud} are the TOA radiance intensities determined from the LUT for a completely clear and a completely cloudy scene, respectively. The scene's effective cloud fraction ($0 \leq f_{ce} \leq 1$) and the cloud pressure p_c are obtained from the Level 2 TEMPO O_2-O_2 cloud retrieval product (Wang et al., 2025). Figure 8 shows the cloud radiance fraction at 440 nm and the cloud pressure used in the calculation of the AMFs for TEMPO's scan 6 on May 9, 2024.

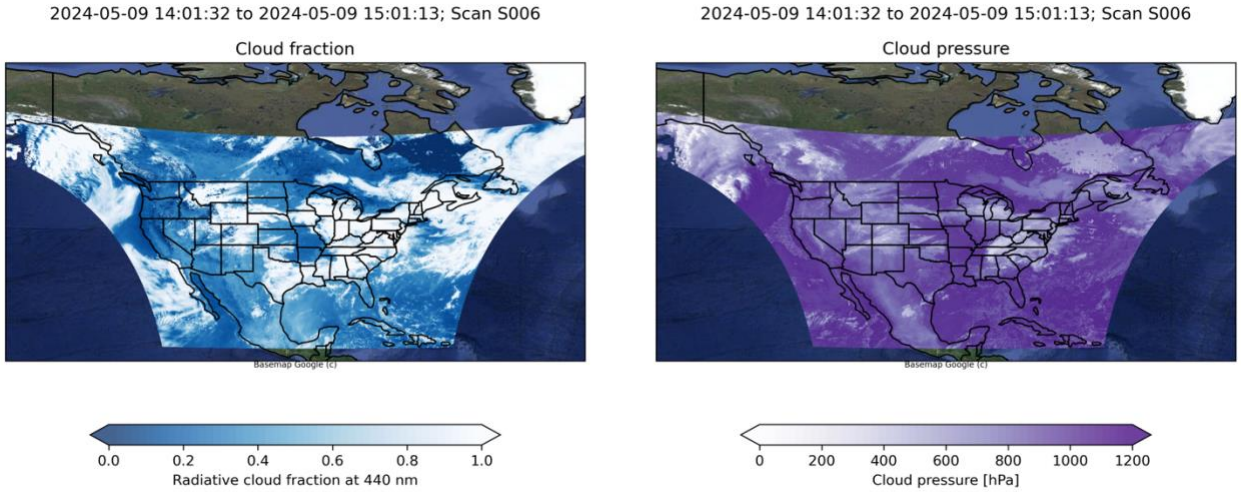

Figure 8. *Cloud radiance fraction and cloud pressure used in the TEMPO NO_2 AMF calculation for scan 6 on May 9, 2024.*

3.1.3.4. Surface Reflectance

For each TEMPO observation, an associated Geometry-dependent surface Lambertian Equivalent Reflectivity (GLER) (Fasnacht et al., 2019; Qin et al., 2019) is calculated. Different GLER derivations are used over land and water. In the version 3 implementation, TEMPO ground pixels are categorized as either land or water using the location of the pixel center. As a result, TEMPO pixels that in reality cover both land and water (i.e., rivers, lakeshores and coastal pixels) do not currently consider mixed surface type GLER.

Over land, the GLER value (albedo) is obtained from two climatologies representing snow-free (α_f) and snow-covered (α_s) scenes. Using information from the 1-km Interactive Multisensor Snow and Ice Mapping System (IMS) product (Helfrich et al., 2018), a final GLER value that can be used as the albedo (α) is determined by weighting with the snow/ice fraction f_s:

$$\alpha = (1 - f_s) \cdot \alpha_f + f_s \cdot \alpha_s. \quad (14)$$

Twenty-two years (2000-2022) of MODIS Bidirectional Reflectance Distribution Function (BRDF) retrievals were used to generate GLER climatologies; the MCD43C1 (Schaaf & Wang, 2015a) and MCD43C2 (Schaaf & Wang, 2015b) v6.1 products are used for snow-covered and

snow-free scenes respectively. Using the derived BRDF climatologies, a set of monthly GLER LUTs were created following the approach of Qin et al. (2019). The land GLER LUTs have a resolution of 0.05° × 0.05° and cover the region of 15° W to 167° W and 14° N to 73° N. The LUTs represent the variation of the GLER during a day by storing values at each location every 30 minutes. The final GLER value is obtained by linear interpolation to the TEMPO observation's time of day and month.

In the case of water, a single GLER is derived from one set of LUTs constructed using the Cox-Munk slope distribution (Cox & Munk, 1954) as described in Fasnacht et al. (2019). The water GLER LUTs are parameterized as function of the wind speed, the time of the day and location. They have a resolution of 1° × 1° and cover 15° W to 167° W and 14° N to 73° N.

Both land and water LUTs are derived at 440 nm. The land LUT at this wavelength is derived using a probabilistic model (factor analysis) that estimates the BRDF at a given wavelength using BRDF observations from the first four MODIS bands (Chan Miller et al., 2019). This model is trained on reflectance spectra from the USGS spectral library (Kokaly et al., 2017) and SCIAMACHY LER (Tilstra et al., 2017) following the methodology described by Zoogman et al. (2016). Figure 9 shows an example of the GLER calculated for TEMPO retrievals at 440 nm.

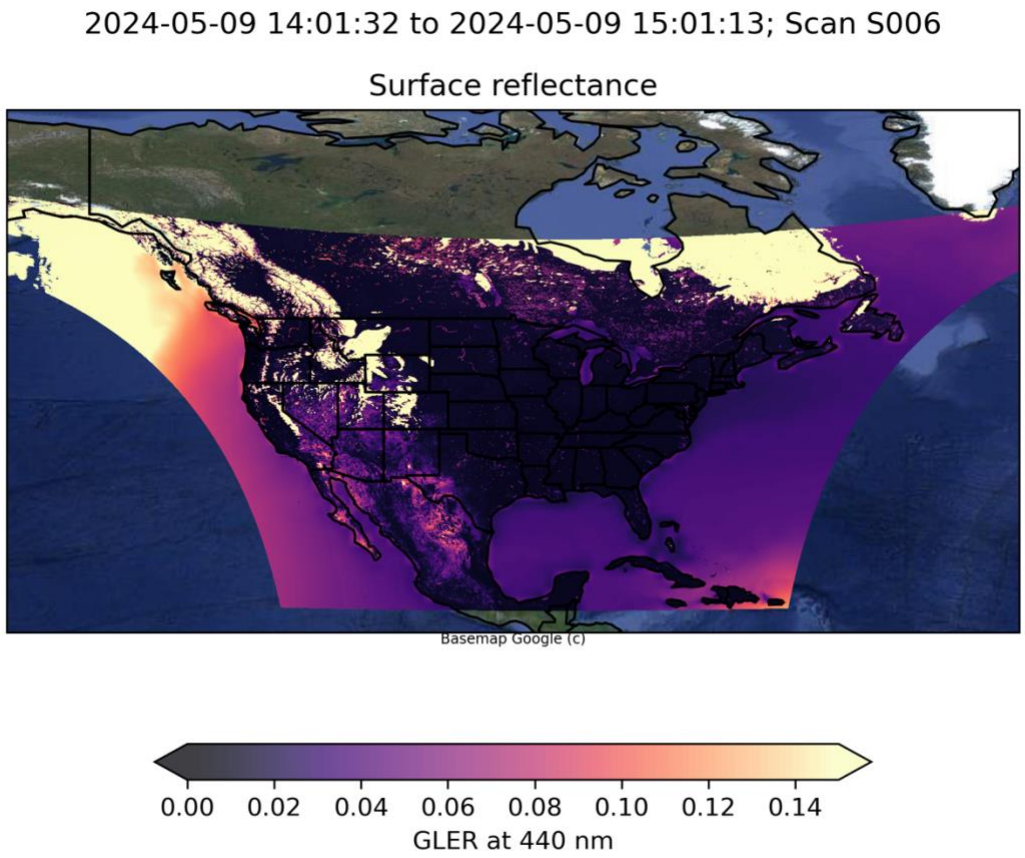

Figure 9. *GLER employed in the calculation of AMFs for TEMPO observations in scan 6 on May 9, 2024. A maximum value of 0.15 in the colormap is chosen to facilitate the perception of details over land not covered by snow and ice.*

3.1.3.5. Atmospheric Model and Trace Gas Profiles

The trace gas algorithm uses atmospheric trace gas profiles and parameters from the Goddard Earth Observing System (GEOS) Composition Forecasting (GEOS-CF) model system (Keller et al., 2021; Knowland, Keller, Wales, et al., 2022). The GEOS-CF is a chemical forecasting system produced by NASA's Global Modeling and Assimilation Office (GMAO). The GEOS-CF system performs near real-time 5-day forecasts of atmospheric composition using the offline GEOS-Chem chemical transport model (http://geos-chem.org) integrated into the GEOS system. Gases and aerosols are simulated at the same resolution as meteorology on a cubed sphere at c360 (~25 km) horizontal resolution and 72 vertical layers from the surface to 0.01 hPa. First, this coupled system is run for the previous 24 hours to have the best initial conditions for the global 5-day forecast produced each day at time 12:00 UTC. Output is saved at high temporal frequency (1 hour) and 0.25° × 0.25° longitude as NetCDF files (Knowland, Keller, & Lucchesi, 2022).

Details on the GEOS-CF system and performance of the version 1.0 tropospheric simulation can be found in Keller et al. (2021). The stratospheric component of the GEOS-CF is described and evaluated in Knowland, Keller, Wales, et al. (2022). The v1.0 implementation, emission inventories and outputs are described in Knowland, Keller, & Lucchesi (2022). GEOS-CF version 1.0 uses gas-phase chemistry simulated with GEOS-Chem version 12.0.1. GEOS-Chem includes detailed HO_x-NO_x-BrO_x-VOC-O_3 tropospheric chemistry (Bey et al., 2001; Mao et al., 2013; Marais et al., 2016; Parrella et al., 2012; Sherwen et al., 2016) of 250 chemical species and coupled stratospheric-tropospheric chemistry (Eastham et al., 2014), with emissions provided by the Harmonized Emissions Component (HEMCO) (Keller et al., 2014). Anthropogenic emissions are from the HTAP (Hemispheric Transport of Air Pollution) (Janssens-Maenhout et al., 2015) and RETRO (REanalysis of the TROposhperic chemical composition) (Schultz et al., 2008) inventories with updated scaling factors (F. Liu et al., 2018; Oda et al., 2018; van der Gon et al., 2011). Biomass burning emissions are determined from the Quick Fire Emission Database (QFED) (Darmenov & da Silva, 2015) using MODIS fire data. Biogenic emissions are determined using MEGAN v2.1 (Model of Emissions of Gases and Aerosols from Nature) (Guenther et al., 2012). Additional emissions are included for lightning and soil NO_x (Hudman et al., 2012; Murray et al., 2012), volcanic SO_2 (Carn, 2019), sea salt aerosols, oceanic emissions of dimethyl sulfide, acetone, acetaldehyde and iodine and soil dust (Knowland, Keller, & Lucchesi, 2022). The 24-hour simulation which serves as the starting point for the next forecast is constrained by the assimilated meteorology from the GEOS Forward Processing for Instrument Teams (FP-IT) (Lucchesi, 2015), a near-real time model system that is comparable to MERRA-2 (Gelaro et al., 2017). GEOS-Chem stratospheric ozone is weakly nudged to ozone from the GEOS-FP, which is constrained by assimilated satellite ozone measurements (Wargan et al., 2015). GEOS-CF version 1.0 does not assimilate any other trace gas or aerosol observations.

To minimize large data transfers and archiving, the GMAO produces a smaller TEMPO-specific GEOS-CF product for use in the TEMPO processing pipeline. Upon completion of each daily GEOS-CF forecast, the most recent GEOS-CF TEMPO forecasts are downloaded to the TEMPO Science Data Processing Center (SDPC). The GEOS-CF TEMPO file is limited in geography to longitudes 180° E to 0° and latitudes 0° to 90° N and contains the vertical mixing ratio profiles of select trace gases detectable in the UV/visible (O_3, NO_2, HCHO, SO_2, H_2O, BrO, $C_2H_2O_2$, HNO_2, IO) and relevant meteorology variables (surface pressure, temperature profile, 2-m eastward and northward winds, tropopause pressure and boundary layer height).

If for any reason GEOS-CF forecasts become unavailable, the TEMPO processing pipeline defaults to using a GEOS-CF climatology provided by GMAO. The climatology consists of monthly averages of the same GEOS-CF trace gas and meteorological variables provided in the GEOS-CF TEMPO daily forecasts. These monthly averages were created using a long-term dataset of GEOS-CF hindcasts from January 2018 to May 2021 (meteorological fields) and January 2020 to May 2021 (chemical fields). The atmospheric profiles and parameters used in the TEMPO processing are created by linearly interpolating between the two monthly

climatologies nearest to the date of the observation. The NO_2 Level 2 file metadata indicates whether a forecast (*apriori_source* = "GEOSCF:forecast") or climatology (*apriori_source* = "GEOSCF:climatology") is used for the atmospheric profiles.

The same 72-layer definition as the GEOS-CF model is used in TEMPO output variables with a vertical dimension. These vertical layers follow a hybrid sigma-pressure grid, with each pressure level at the boundary of a layer defined by a set of fixed Eta coefficients, *eta_a* and *eta_b*, which are a function of layer number. The bottom boundary of a layer *i* is defined as

$$p_i = eta\_a_i + p_s \cdot eta\_b_i \tag{15}$$

with the top of the layer defined as

$$p_{i+1} = eta\_a_{i+1} + p_s \cdot eta\_b_{i+1}. \tag{16}$$

In combination with the surface pressure p_s, the Eta coefficients can be used to reconstruct the vertical pressure grid for each TEMPO observation. The Eta coefficients are provided in Level 2 TEMPO trace gas files as attributes of the surface pressure variable.

Figure 7 shows examples of NO_2 vertical profiles simulated by GEOS-CF for "clean" and "polluted" ground pixels, while Figure 10 shows an example of the partial column of the lowermost layer (~120 m thickness at standard surface pressure) of the GEOS-CF simulation.

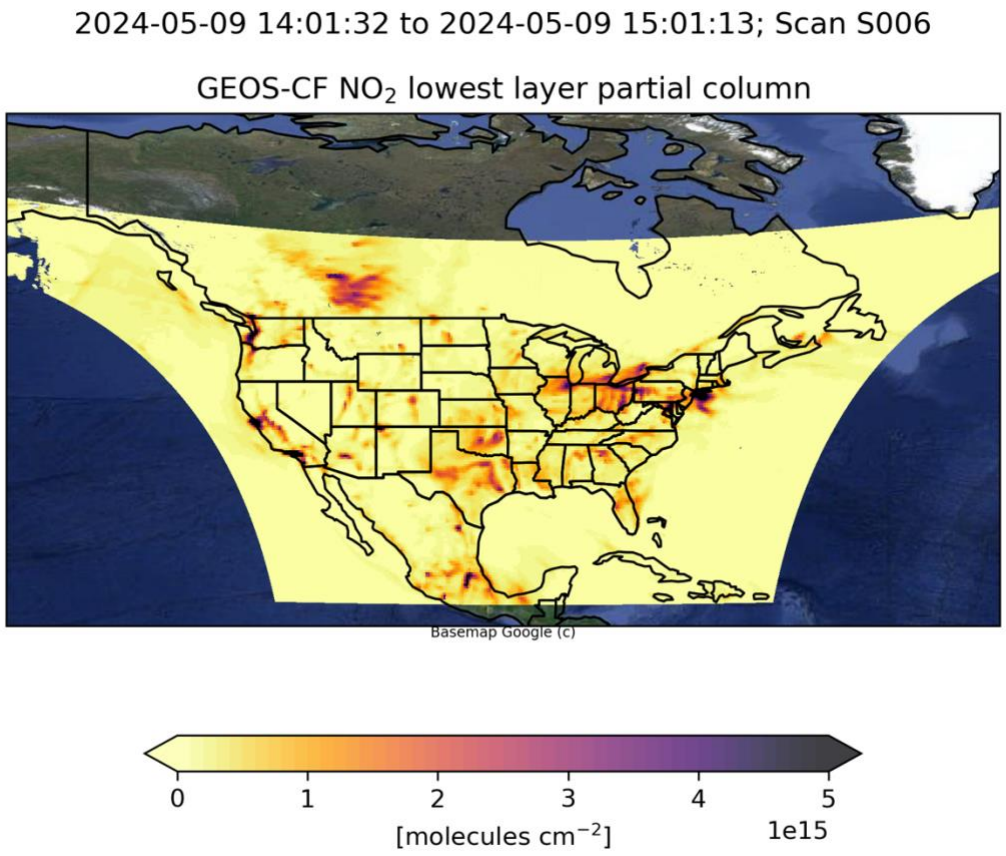

Figure 10. *Partial column of NO_2 in the lowermost (surface) layer for scan 6 on May 9, 2024, simulated by the GEOS-CF forecasting system.*

3.1.3.6. Terrain Pressure Correction

The use of an atmospheric model with coarser spatial resolution than the satellite observations can lead to significant errors in the AMF in areas of inhomogeneous terrain elevation (Boersma et al., 2011; Zhou et al., 2009). In order to correct for terrain height inhomogeneities over the model grid cell, the surface pressure and atmospheric profiles are corrected using the effective terrain height for each satellite ground pixel as determined from the GMTED2010 high resolution digital elevation model (DEM) (Danielson & Gesch, 2011). This correction uses the hypsometric equation with linear temperature lapse rate (Zhou et al., 2009). The effective surface pressure $p_{s,obs}$ for each satellite observation is given by

$$p_{s,obs} = p_{s,model} \times \left[\frac{T_s}{T_s + \Gamma(h_{model} - h_{DEM})}\right]^{-g/R\Gamma} \quad (17)$$

where $p_{s,model}$ is the surface pressure from the coincident model grid cell, T_s is the corresponding

surface temperature, h_{model} is the terrain altitude from the model, h_{DEM} is the effective terrain altitude derived from the DEM, Γ = 6.5 K m^{-1} is the temperature lapse rate, R = 287 J kg^{-1} K^{-1} is the gas constant of dry air, and g = 9.81 m s^{-2} is Earth's acceleration of gravity. Pressure levels for other layers are then adjusted using the Eta coefficients as described in the equations defining the pressure levels. While the surface and layer pressures and resulting air column change, trace gas mixing ratio profiles are conserved in each altitude layer.

3.1.3.7. Temperature Correction

The molecular absorption cross section of NO_2 is temperature-dependent and the algorithm needs to consider the atmospheric temperature profile in order to avoid introducing additional errors through the use of a single NO_2 cross section collected at one temperature in the slant column density retrieval (Boersma et al., 2004; Bucsela et al., 2013). This is done by applying a layer-dependent correction factor *c(z)* as part of the AMF calculation, as previously noted in Section 3.1.3.1. The TEMPO algorithm applies the correction determined empirically for the TROPOMI NO_2 AMF calculation, which uses the same wavelength fitting window of 405 - 465 nm (van Geffen, Eskes, Boersma, et al., 2022). The correction for a given layer is defined as

$$c(z) = 1 - 0.00316[T(z) - T_\sigma] + 3.39 \times 10^{-6}[T(z) - T_\sigma]^2, \quad (18)$$

where *T(z)* is the temperature at layer *z* from the GEOS-CF forecast, and T_σ is the temperature of the NO_2 absorption cross section used in the spectral fitting (220 K).

3.1.3.8. Accounting for Aerosol Effects

Aerosols affect the light path of a photon through the atmosphere, and as a result, their presence in a scene will influence the altitude dependent scattering weights and the AMF. The effect of aerosols depends on their altitude and optical properties (Leitão et al., 2010):

- Non-absorbing aerosols increase sensitivity to the trace gas within and above the aerosol layer through an increase in scattering probability and photons returned from these altitudes. The sensitivity within a layer is also increased due to multiple scattering.
- Non-absorbing aerosols decrease sensitivity below the aerosol layer as they prevent photons from penetrating to lower altitudes.
- Absorbing aerosols decrease sensitivity below and within the aerosol layer by decreasing the total light path.

Aerosols are not currently considered explicitly in the AMF calculation, but the effect is implicitly accounted for through the use of TEMPO-retrieved cloud radiance fractions and cloud pressures. They are considered as a source of uncertainty in the final NO_2 product.

3.1.4. Stratosphere-Troposphere Separation

Stratosphere-troposphere separation follows the methodology described by Geddes et al. (2018), adapted to TEMPO's operational environment. The initial estimate of the stratospheric NO_2 vertical column ($V_{strat,init}$) is

$$VCD_{strat,init} = \frac{\left(SCD - SCD_{trop,prior}\right)}{AMF_{strat}} \tag{19}$$

where SCD is the retrieved total slant column density, AMF_{strat} is the stratospheric air mass factor, and $SCD_{trop,prior}$ represents prior knowledge of tropospheric contributions to the total slant column density. The $SCD_{trop,prior}$ is determined from the calculated tropospheric air mass factor (AMF_{trop}) and the tropospheric vertical column density ($VCD_{trop,prior}$) obtained by integrating the GEOS-CF forecast's NO_2 column from the surface to the tropopause using

$$SCD_{trop,prior} = VCD_{trop,prior} \cdot AMF_{trop}. \tag{20}$$

There may be biases in the initial stratospheric vertical column ($V_{strat,init}$) in ground pixels where the tropospheric prior (forecast) is high. These pixels are masked following the approach of Bucsela et al. (2013), by requiring:

$$\frac{SCD_{trop,prior}}{AMF_{strat}} < 0.3 \times 10^{15} \text{ molecules cm}^{-2}. \tag{21}$$

The remaining unmasked data are then binned to a 0.1° x 0.1° grid and smoothed. For the smoothing step, a boxcar filter is applied with a moving 15° longitude x 10° latitude window using

$$B_i = \frac{1}{w}\sum_{j=0}^{w-1} A_{i+j-w/2} \tag{22}$$

where

$$\frac{w-1}{2} \le i \le N - \frac{w+1}{2}. \tag{23}$$

Here, w is the smoothing width in grid-space (defined in this case by both a length and width), B_i is the i^{th} point in the smoothed data, and A_i is the i^{th} point in the original masked data. In the case where the window includes points outside the FOR, the nearest edge points are used. In a

subsequent step, any values that lie more than 1.5 standard deviations outside the window average are removed through two passes of the boxcar filter.

A 30° longitude x 20° latitude moving window is then used to fill missing bins. To obtain the final stratospheric NO_2 column estimate (VCD_{strat}), another boxcar smoothing step with a 5° longitude x 3° latitude window is then applied, and the gridded data are interpolated back to the observation footprints.

Operationally, the stratosphere-troposphere separation is performed after the spectral fitting and AMF calculation of all Level 2 granules in one TEMPO East-West scan are complete. This ensures the availability of the SCDs and AMFs over a large area for the separation calculation. Figure 11 shows an example of NO_2 tropospheric and stratospheric columns derived using the stratosphere-troposphere separation algorithm.

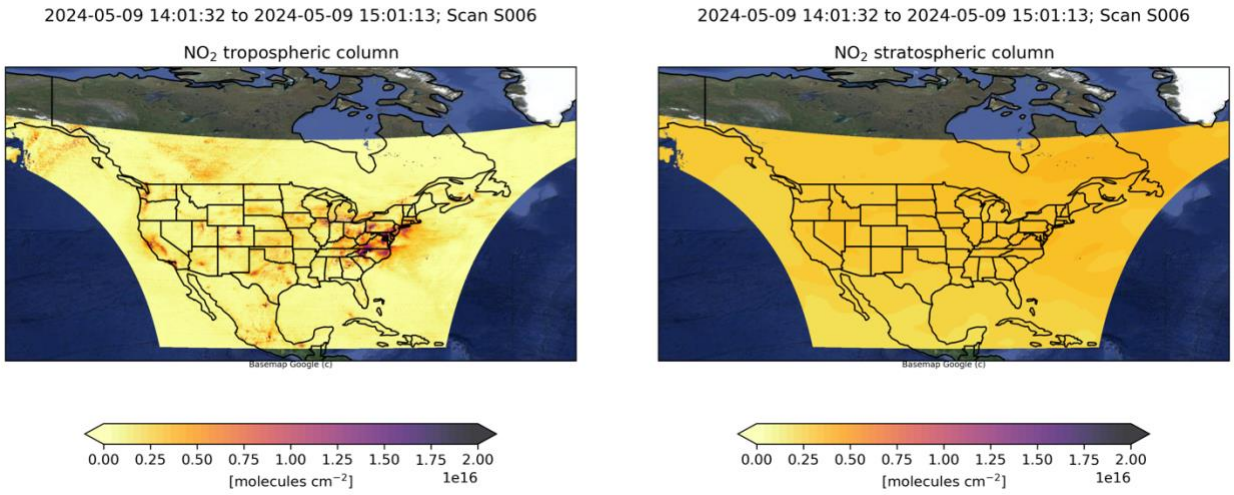

Figure 11. *NO_2 tropospheric and stratospheric vertical columns for scan 6 on May 9, 2024, derived using the stratosphere-troposphere separation algorithm. The tropospheric columns are the same as those shown in Figure 1 but have not been filtered by cloud fraction.*

3.1.5. Scientific Theory Assumptions

Several assumptions are made in the derivation of version 3 NO_2 vertical column densities:

1) Slant column density retrieval

- The atmospheric absorption of trace gases is optically thin.
- The wavelength dependency of the surface reflectance, aerosol effects and calibration issues can be approximated with low-order polynomials.

2) Air mass factor calculation

- Clouds are considered as Lambertian surfaces with an albedo of 0.8.
- The independent pixel approximation is used, which considers each ground pixel to be composed of a clear-sky and cloudy-sky part.
- The air mass factor is assumed to be constant through the fitting window and is calculated at 440 nm.
- All water bodies are treated as open ocean for the surface reflectance calculation, and shallow water/turbidity is not considered. The current algorithm treats ground pixels as either land or water, and mixed surface types are not currently considered.
- Several assumptions are made in the use of the GLER for surface reflectance, including that the surface reflectance on a given day is accurately represented by a 22-year MODIS climatology which uses kernels to approximate BRDFs, and that GLER based on MODIS can be used at the more extreme viewing angles of geostationary orbit.
- The output a priori trace gas profiles from the chemical transport model are considered as "truth".
- Aerosols are considered implicitly through the use of retrieved cloud fraction and pressure.

3) Stratosphere-troposphere separation

- The stratospheric NO_2 field is assumed to be smoothly varying.
- The GEOS-CF tropopause pressure is assumed to be correct.

3.2. Algorithm Input Variables

Table 8. *Algorithm input variables*

Name	Long Name	Unit
product/cloud_fraction	effective cloud fraction from file TEMPO_CLDO4_L2	unitless
product/cloud_pressure	cloud pressure from file TEMPO_CLDO4_L2	hPa
band_290_490_nm/irradiance	irradiance from file TEMPO_IRR_L1	photons/s/cm^2/nm
band_290_490_nm/pixel_quality_flag	pixel quality flag from file TEMPO_IRR_L1	unitless
band_290_490_nm/sf_asym	slit function asymmetry parameter from file TEMPO_IRR_L1 (not currently applied in v3)	unitless
band_290_490_nm/sf_hw1e	slit function half-width at 1/e parameter from file TEMPO_IRR_L1 (not currently applied in v3)	nm
band_290_490_nm/sf_shape	slit function shape parameter from file TEMPO_IRR_L1 (not currently applied in v3)	unitless
band_290_490_nm/wavecal_params	wavelength calibration parameters from file TEMPO_IRR_L1	nm
band_290_490_nm/ground_pixel_quality_flag	ground pixel quality flag from file TEMPO_RAD_L1	unitless
band_290_490_nm/inr_quality_flag	INR quality flag from file TEMPO_RAD_L1	unitless
band_290_490_nm/latitude	latitude from file TEMPO_RAD_L1	degrees_north
band_290_490_nm/latitude_bounds	latitude bounds (NE,NW,SW,SE) from file TEMPO_RAD_L1	degrees_north
band_290_490_nm/longitude	longitude from file TEMPO_RAD_L1	degrees_east
band_290_490_nm/longitude_bounds	longitude bounds (NE,NW,SW,SE) from file TEMPO_RAD_L1	degrees_east
band_290_490_nm/pixel_quality_flag	pixel quality flag from file TEMPO_RAD_L1	unitless
band_290_490_nm/radiance	radiance from file	photons/s/cm^2/nm/sr

	TEMPO_RAD_L1	
band_290_490_nm/snow_ice_fraction	snow ice fraction from file TEMPO_RAD_L1	unitless
band_290_490_nm/solar_azimuth_angle	solar azimuth angle from file TEMPO_RAD_L1	degrees
band_290_490_nm/solar_zenith_angle	solar zenith angle from file TEMPO_RAD_L1	degrees
band_290_490_nm/terrain_height	area-weighted mean terrain height from file TEMPO_RAD_L1	m
band_290_490_nm/viewing_azimuth_angle	viewing azimuth angle from file TEMPO_RAD_L1	degrees
band_290_490_nm/viewing_zenith_angle	viewing zenith angle from file TEMPO_RAD_L1	degrees
band_290_490_nm/wavecal_params	wavelength calibration parameters from file TEMPO_RAD_L1	nm
earth_sun_distance	Earth-sun distance from file TEMPO_RAD_L1	m
mirror_step	scan mirror position index from file TEMPO_RAD_L1	unitless
time	exposure start time from file TEMPO_RAD_L1	seconds since 1980-01-06T00:00:00Z
NO2	Nitrogen dioxide (NO2, MW = 46.00 g mol-1) volume mixing ratio dry air from file GEOS-CF	mol/mol
O3	Ozone (O3, MW = 48.00 g mol-1) volume mixing ratio dry air from file GEOS-CF	mol/mol
PHIS	surface geopotential height from file GEOS-CF	m^2/s^2
PS	surface pressure from file GEOS-CF	Pa
T	air temperature from file GEOS-CF	K
TROPPB	tropopause pressure based on blended estimate from file GEOS-CF	Pa
U2M	2-meter eastward wind from file GEOS-CF	m/s
V2M	2-meter northward wind from file GEOS-CF	m/s

lat	latitude from file GEOS-CF	degrees_north
lon	longitude from file GEOS-CF	degrees_east
Ap	Eta a coefficients from GEOS-Chem_72_layer_vertical_grid .nc	unitless
Bp	Eta b coeffficients from GEOS-Chem_72_layer_vertical_grid .nc	unitless
alb	albedo from GLER land/snow/ocean files	unitless
doy	day of year from GLER land/snow/ocean files	unitless
hour	hour from GLER land/snow/ocean files	hour
lat	latitude from GLER land/snow/ocean files	degrees_north
lon	longitude from GLER land/snow/ocean files	degrees_east
qf	quality flag from GLER land/snow/ocean files	unitless
Grid/Albedo	albedo nodes from AMF LUT file	unitless
Grid/OZO	ozone nodes AMF LUT file	string
Grid/Surface_Pressure	surface pressure nodes from AMF LUT file	hPa
Grid/SZA	solar zenith angle nodes from AMF LUT file	degrees
Grid/VZA	viewing zenith angle nodes from AMF LUT file	degrees
Grid/Wavelength	wavelength from AMF LUT file	nm
Intensity/I0	radiance I_0 from AMF LUT file	W/cm^2
Intensity/I1	radiance I_1 from AMF LUT file	W/cm^2
Intensity/I2	radiance I_2 from AMF LUT file	W/cm^2
Intensity/Ir	radiance I_r from AMF LUT file	W/cm^2
Intensity/Sb	multiple surface reflection term from AMF LUT file	unitless

Profiles/Air_Column_Layer	air column layer from AMF LUT file	molecules/cm^2
Profiles/Altitude_Layer	altitude layer from AMF LUT file	km
Profiles/Altitude_Level	altitude level from AMF LUT file	km
Profiles/Ozone_Column_Layer	ozone column layer from AMF LUT file	molecules/cm^2
Profiles/Pressure_Layer	pressure layer from AMF LUT file	hPa
Profiles/Pressure_Level	pressure level from AMF LUT file	hPa
Profiles/Temperature_Level	temperature level from AMF LUT file	K
Scattering_Weights/dI0	scattering weights from AMF LUT file	unitless
Scattering_Weights/dI1	scattering weights from AMF LUT file	unitless
Scattering_Weights/dI2	scattering weights from AMF LUT file	unitless

3.3. Algorithm Output Variables

Table 9. *Algorithm output variables*

Name	Long Name	Unit
geolocation/latitude	pixel center latitude	degrees_north
geolocation/latitude_bounds	pixel corner latitude	degrees_north
geolocation/longitude	pixel center longitude	degrees_east
geolocation/longitude_bounds	pixel corner longitude	degrees_east
geolocation/relative_azimuth_angle	relative azimuth angle at pixel center	degrees
geolocation/solar_azimuth_angle	solar azimuth angle at pixel center	degrees
geolocation/solar_zenith_angle	solar zenith angle at pixel center	degrees
geolocation/time	radiance exposure start time	seconds since 1980-01-06T00:00:00Z
geolocation/viewing_azimuth_angle	viewing azimuth angle at pixel center	degrees
geolocation/viewing_zenith_angle	viewing zenith angle at pixel center	degrees
product/main_data_quality_flag	main data quality flag	unitless
product/vertical_column_stratosphere	stratosphere nitrogen dioxide vertical column	molecules/cm^2
product/vertical_column_troposphere	troposphere nitrogen dioxide vertical column	molecules/cm^2
product/vertical_column_troposphere_uncertainty	troposphere nitrogen dioxide vertical column uncertainty	molecules/cm^2
qa_statistics/fit_convergence_flag	radiance fit convergence flag	unitless
qa_statistics/fit_rms_residual	radiance fit RMS residual	unitless
support_data/albedo	surface albedo	unitless
support_data/amf_cloud_fraction	cloud fraction	unitless
support_data/amf_cloud_pressure	cloud pressure	hPa
support_data/amf_diagnostic_flag	nitrogen dioxide air mass factor diagnostic flag	unitless
support_data/amf_stratosphere	nitrogen dioxide stratospheric air mass factor	unitless
support_data/amf_total	nitrogen dioxide air mass factor	unitless
support_data/amf_troposphere	nitrogen dioxide	unitless

	tropospheric air mass factor	
support_data/eff_cloud_fraction	effective cloud fraction	unitless
support_data/fitted_slant_column	nitrogen dioxide fitted slant column	molecules/cm^2
support_data/fitted_slant_column_uncertainty	nitrogen dioxide fitted slant column uncertainty	molecules/cm^2
support_data/gas_profile	vertical profile of nitrogen dioxide partial column	molecules/cm^2
support_data/ground_pixel_quality_flag	ground pixel quality flag	unitless
support_data/scattering_weights	scattering weights	unitless
support_data/snow_ice_fraction	fraction of pixel area covered by snow and/or ice	unitless
support_data/surface_pressure	surface pressure	hPa
support_data/temperature_profile	air temperature	K
support_data/terrain_height	terrain height	m
support_data/tropopause_pressure	tropopause pressure	hPa
support_data/vertical_column_total	nitrogen dioxide vertical column	molecules/cm^2
support_data/vertical_column_total_uncertainty	nitrogen dioxide vertical column uncertainty	molecules/cm^2
mirror_step	scan mirror position index	unitless
xtrack	pixel index along slit	unitless

4. Algorithm Usage Constraints

4.1. Data Filtering

Users of the trace gas products should at minimum apply filtering of the data considering the main data quality flag and cloud fraction. For the majority of users of version 3 NO_2, we recommend using only data where *main_data_quality_flag* = 0 and *eff_cloud_fraction* < 0.2. Note that Level 3 products (gridded data for the entire scan) are not pre-filtered, and the same filtering recommendations apply to Level 3.

The *main_data_quality_flag* variable in the *product* group of the Level 2 and Level 3 files provides a high-level approximation to product quality. Table 10 provides the definition of the *main_data_quality_flag* for NO_2 retrievals. Further details on data usage, known issues and file structure may be found in the TEMPO Trace Gas and Cloud Level 2 and 3 Data Products User Guide (González Abad et al., 2024) available at https://asdc.larc.nasa.gov/project/TEMPO.

Table 10. *Logic employed to set the values of the* main_data_quality_flag *for version 3 TEMPO data. The variable* fit_convergence_flag *is provided in the* qa_statistics *group of the Level 2 files. The values of* amf_diagnostic_flag, *AMF_{total}, VCD_{total} and SCD_{uncert} are provided in the* support_data *group (while most users will be interested in the NO_2 tropospheric and stratospheric VCDs, the total NO_2 VCD and its uncertainty are used in the determination of the main data quality flag for simplicity and consistency with other molecules derived using the trace gas code). The geometric air mass factor is calculated as AMF_{geo} = sec(SZA) + sec(VZA).*

Value	Name	Description	
0	normal	fit_convergence_flag = 1	AND
		-10^{19} molecules $cm^{-2} \leq VCD_{total} \leq 10^{19}$ molecules cm^{-2}	AND
		$(SCD + 2*SCD_{uncert}) \geq 0$	AND
		$AMF_{geo} \leq 6$	AND
		$AMF_{total} \geq 0.1$	
1	suspicious	fit_convergence_flag = 0	OR
		$(SCD + 2*SCD_{uncert}) < 0$ *AND* $(SCD + 3*SCD_{uncert}) \geq 0$	OR
		$VCD_{total} < -10^{19}$ molecules cm^{-2}	OR
		$VCD_{total} > 10^{19}$ molecules cm^{-2}	OR
		$AMF_{geo} > 6$	OR
		$AMF_{total} < 0.1$	
2	bad	fit_convergence_flag < 0	OR
		$(SCD + 3*SCD_{uncert}) < 0$	OR
		amf_diagnostic_flag(bit1) = 1	

Retrievals of the highest quality have a *main_data_quality_flag* equal to “0”. This flag considers the value of the VCDs to detect outliers, the viewing geometry for each pixel and the availability of a successful AMF calculation. Owing to increased uncertainties in the spectral fitting and AMF calculations, pixels with geometric AMF (AMF_{geo}) larger than 6 (SZA > ~70° and VZA > ~70°) are categorized as “suspicious” with *main_data_quality_flag* equal to “1”. Pixels categorized as suspect carry useful information, but their interpretation requires further analysis. Fitting uncertainties in early and late hours of the day increase, and the sensitivity of TEMPO to lower tropospheric NO_2 is reduced. Those pixels identified as outliers or without a successful AMF calculation are categorized as "bad" with a *main_data_quality_flag* value equal to “2”.

TEMPO NO_2 measurements should also be filtered by cloud fraction for several reasons. First, clouds obscure the lower atmosphere, leading to less sensitivity to the column near the surface and larger uncertainties, even for high quality radiance observations. In addition, version 3 NO_2 spectral fitting is known to degrade over partly cloudy pixels due to the inhomogeneous illumination of the instrument slit, resulting in large fitting uncertainties in the retrieved SCD in these partly cloudy scenes. Finally, the version 3 cloud fraction product is known to have a high bias due to a Level 1B overestimation of the absolute radiance and probably errors in the GLER (Wang et al., 2025). In consequence, the recommendation is to use only the highest quality retrievals by limiting analyses to pixels with effective cloud fractions (*support_data/eff_cloud_fraction*) < 0.2. More strict cloud fraction criterion (e.g., < 0.15) will retain less data, though the retained data will have less cloud influence. Users are thus advised to adjust based on their tolerance. This cloud fraction recommendation is for the current data version 3, and the cloud filter recommendation may change for future data releases.

GLER look-up-table accuracy is difficult to assess, particularly over snow and ice, bright surfaces, and quality of the MODIS product for TEMPO geometries. We recommend using the *snow_ice_fraction* in the *support_data* group to identify pixels covered by snow and ice and treat them with care.

The *geolocation* and *support_data* groups contain variables necessary to interpret the observations. The *support_data/amf_diagnostic_flag* is a 16-bit bitwise flag indicating different assumptions/issues in the air mass factor calculation, which advanced users may wish to consult for further insight. Table 11 provides the meaning of each bit in the *amf_diagnostic_flag*.

Table 11. *Meaning of each bit of* amf_diagnostic_flag *in Level 2 NO_2 files*

Bit	Bit Meaning
bit0	Good AMF
bit1	Bad AMF / no AMF calculation performed
bit2	Warning: pixel affected by glint
bit3	Warning: climatological cloud pressure information used
bit4	Warning: adjusted surface pressure (original surface pressure outside LUT bounds)
bit5	Warning: adjusted cloud pressure (original cloud pressure outside LUT bounds)
bit6	Not used / reserved for future use
bit7	Not used / reserved for future use
bit8	Not used / reserved for future use
bit9	Not used / reserved for future use
bit10	Error: no albedo information
bit11	Error: no cloud information
bit12	Error: no trace gas profile information
bit13	Error: no scattering weight calculation
bit14	Error: no geolocation information available
bit15	Not used / reserved for future use

4.2. Use of NO_2 Total Columns

Most users who wish to use the total NO_2 column (for instance, for comparisons with total NO_2 measured by ground-based Pandora instruments) should use the sum of *vertical_column_troposphere + vertical_column_stratosphere* in the main *product* group. The *vertical_column_total* in the *support_data* group is determined using the full profile of scattering weights and full model GEOS-CF profile and is significantly influenced by the relative model amounts of the stratospheric and tropospheric profile, and its use by most users is discouraged.

5. Performance Assessment

5.1. Validation Methods

The TEMPO NO_2 validation plan and methods are described in the Level 2 Science Data Product Validation Plan (TEMPO Validation Team, 2023). The validation plan outlines a validation approach to meet the Program Level Requirements Appendix (PLRA) baseline requirement for TEMPO NO_2 validation and to extend the validation in a best effort approach to leverage measurement and modeling assets over the TEMPO baseline mission. This includes the use of ground-based and satellite observations for routine validation, as well as dedicated and episodic field missions. The TEMPO validation plan defines three levels of product maturity:

1. **Beta**: Product is minimally validated but may contain significant errors. Publication of studies that use these data is discouraged.
2. **Provisional**: Product performance has been demonstrated through a large, but still (seasonally or otherwise) limited number of independent measurements. Product is potentially ready for operational users and may be suitable for scientific publication.
3. **Full**: Product performance has been demonstrated over a large and wide range of representative conditions, with comprehensive documentation of product performance, including known anomalies and their remediation strategies. Products are ready for systematic use and covering the full range of scientific and application use and publication.

Some correlative datasets that can be used for routine assessment of TEMPO NO_2 are included in Table 12.

Table 12. *Datasets for routine assessment of TEMPO NO_2*

Dataset	Description	Website
PGN	Network of Pandora spectrometers (Direct Sun and MAX-DOAS geometry)	http://pandonia-global-network.org
S5P TROPOMI NO_2	NO_2 retrievals from Sentinel-5P TROPOMI satellite instrument	https://disc.gsfc.nasa.gov/datasets/S5P_L2__NO2____HiR_2/summary
NDACC	DOAS UV-Visible zenith sky spectrometers	http://ndacc.org
AQS	in-situ surface NO_2	https://aqs.epa.gov

In addition to these datasets, TEMPO NO_2 will be intercompared with NO_2 from the LEO satellite instrument OMI. Multiple field campaigns that include airborne in situ and remote sensing instruments are occurring during the TEMPO baseline mission, providing valuable data for TEMPO validation. These include Synergistic TEMPO Air Quality Science (STAQS),

Atmospheric Emissions and Reactions Observed from Megacities to Marine Areas (AEROMMA), Coastal Urban Plume Dynamics Study (CUPiDS), and the Northeast Corridor Air Quality and Greenhouse Gas (NEC-AQ-GHG) Study. These campaigns occurred during Summer 2023, overlapping with the first month of TEMPO operations. Additional campaigns with TEMPO validation components are anticipated for future years, including summer Student Airborne Research Program (SARP) flights and the Hemispheric Airborne Measurements of Air Quality (HAMAQ), anticipated in Summer 2028.

The TEMPO validation team carried out a series of comprehensive validation studies during the first year of TEMPO operations. Based on the results of these studies, the NO_2 version 3 product has been declared at provisional maturity level. Users should refer to the TEMPO validation report (TEMPO Validation Team, 2025) for detailed validation results.

5.2. Uncertainties

Due to their ability to measure the NO_2 column with high temporal frequency and over long time periods, Pandora instruments in the PGN (Pandonia Global Network) form the core network for TEMPO NO_2 validation. Models such as WRF-Chem and CMAQ may also be used as intercomparison platforms for non-coincident validation measurements. Uncertainties of the correlative datasets vary. Details of these uncertainties are included in the Validation Plan (TEMPO Validation Team, 2023) or in individual dataset references.

5.3. Validation Errors

The NO_2 Level 2 product provides slant column and vertical column random uncertainties derived from the spectral fitting of the slant column density. Figure 12 shows the distribution of TEMPO VCD fitting uncertainties for scan 6 on May 9, 2024. The red vertical line indicates the mission requirement precision, defined for four co-added observations. TEMPO NO_2 far exceeds the mission precision requirement, with the large majority of TEMPO single pixel observations having less uncertainty than the required precision of four co-added pixels. In the current version 3 retrievals, the precision of the retrieval does degrade in the presence of clouds due to the inhomogeneous illumination of the instrument slit in partly cloudy scenes.

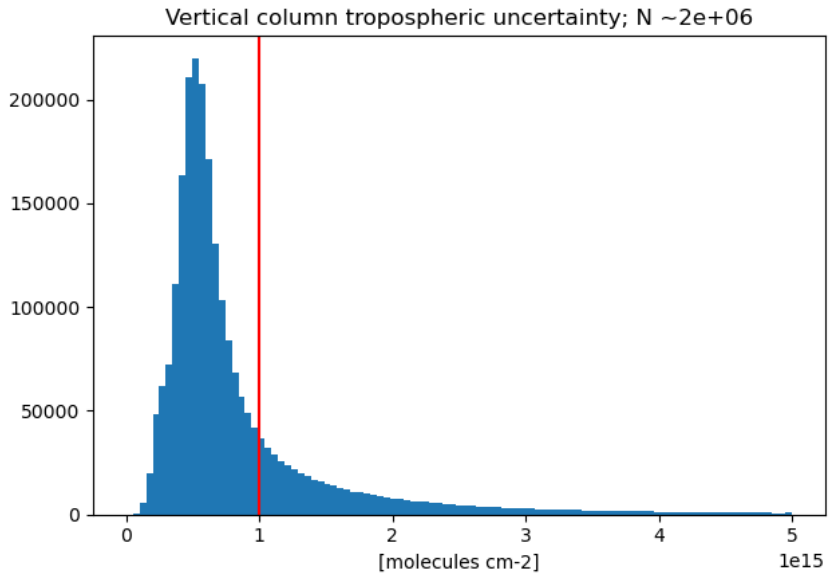

Figure 12. *Histogram of TEMPO NO_2 vertical column uncertainty (precision) included in the Level 2 files for scan 6 on May 9, 2024 (14:01:32 - 15:01:13 UTC). All cloud fractions are included in the histogram. The vertical red line marks the TEMPO mission requirement of 1×10^{15} molecules cm^{-2} for four co-added ground pixels.*

Systematic errors in the SCD can result from model parameter errors and instrumental effects. The magnitude of these impacts is currently being investigated for TEMPO SCDs, but likely range on the order of a few percent. The current version 3 data additionally show North/South striping in the SCD (the across-track direction), as is frequently seen in remote sensing instruments utilizing CCD array detectors. These stripes are estimated to be on the order of $\pm5\times10^{14}$ molecules cm^{-2}. The implementation of a de-striping correction in a later version is anticipated.

Systematic errors in the VCD tend to be dominated by uncertainties in the AMF calculation, and in most cases result primarily from uncertainties in surface albedo, cloud parameters, and trace gas profiles. Lorente et al. (2017) performed detailed comparisons of multiple OMI NO_2 retrievals from different algorithm groups and estimated an overall structural uncertainty in the AMF due to the use of different ancillary data inputs to be on average 42% over polluted regions and 31% over unpolluted regions. The most significant impacts were from trace gas profiles, surface albedo and clouds. The lack of an explicit aerosol correction in the trace gas retrievals can also cause large errors in the AMF under high aerosol loading conditions. Potential errors can be particularly large in biomass burning plumes. Based on previous studies (Castellanos et al., 2015; Griffin et al., 2021), we estimate TEMPO NO_2 in biomass burning plumes to have systematic uncertainties on the order of 20 to 50%, with even larger errors in some cases (>100%) due to the exclusion of aerosols in the AMF calculation.

The performance of TEMPO AMF calculations at high solar zenith angles (above 70°) still needs to be assessed after addressing uncertainties associated with GLER LUTs and non-spherical scattering weights. However, Figure 13, showing the dependency of the fitting uncertainty with solar zenith angle, suggests that TEMPO SCDs at least may be useful beyond 70°.

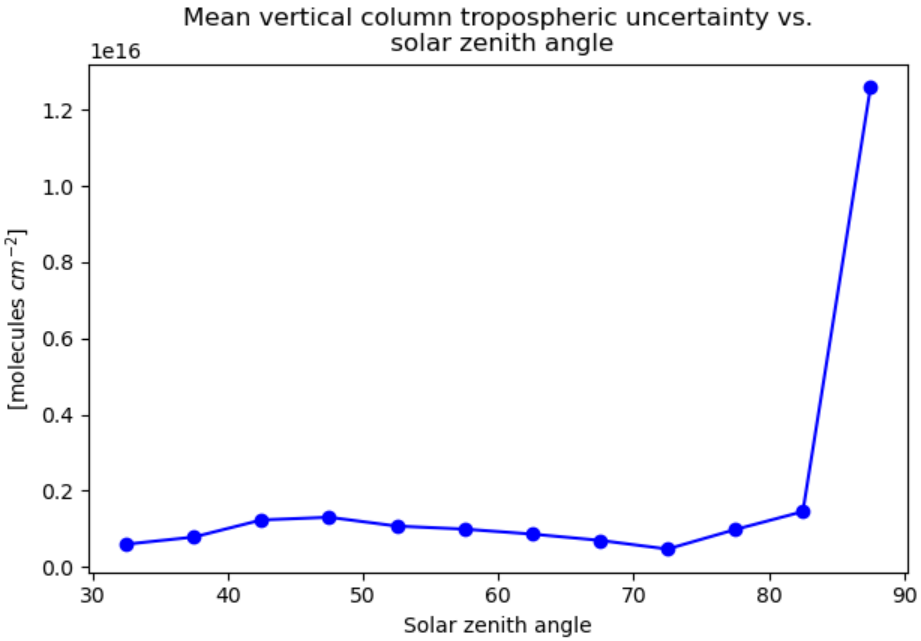

Figure 13. *TEMPO NO_2 vertical column fitting uncertainty as a function of solar zenith angle for retrievals performed for scan 6 on May 9, 2024 (14:01:32 - 15:01:13 UTC).*

The current version 3 TEMPO retrievals have a high bias in the retrieved effective cloud fraction determined in the cloud algorithm (Wang et al., 2025), which will propagate errors to the final trace gas products in clear (cloud-free) skies. This is likely caused by a combination of a high bias in the L1B calibrated radiances and biases in the GLER, which both affect the cloud fraction retrieval. Biases in the GLER will also affect the trace gas retrievals directly by introducing error in the calculation of the scattering weights. In most cases, the high bias in cloud fraction will result in a high bias in the retrieved tropospheric NO_2 column in polluted areas.

Uncertainties in the stratosphere-troposphere separation result from uncertainties in the various inputs to the stratosphere-troposphere separation algorithm, including the uncertainties discussed above in the SCD and AMF, as well as the tropopause height taken from the GEOS-CF forecast. Bucsela et al. (2013) estimated the total uncertainty in OMI NO_2 stratosphere-troposphere separation to be on the order of 0.2 x 10^{15} molecules cm^{-2}, based on uncertainties from the three largest error contributions ($SCD_{trop,prior}$, AMF_{trop} and uncertainties in interpolating VCD_{strat} in masked regions), with errors slightly larger in masked polluted regions and much smaller in clean areas. The TEMPO stratosphere-troposphere separation algorithm is based on that of OMI,

and similar uncertainties are expected for nominal hourly scans of the full FOR (Geddes et al., 2018).

The quantification of on-orbit precision and accuracy from validation activities is an ongoing effort led by TEMPO's validation team. Please refer to TEMPO validation report (TEMPO Validation Team, 2025) for a detailed analysis of TEMPO NO_2 performance.

6. Algorithm Implementation

6.1. Algorithm Availability

The TEMPO nitrogen dioxide algorithm has been integrated into the TEMPO Science Data Processing Center (SDPC) pipeline at the Smithsonian Astrophysical Observatory. SDPC v4.4 is used to produce the version 3 data that was publicly released in May 2024.

6.2. Input Data Access

URL	Description
https://dx.doi.org/10.5067/IS-40e/TEMPO/IRR_L1.003	TEMPO Level 1B Irradiance Product
https://dx.doi.org/10.5067/IS-40e/TEMPO/RAD_L1.003	TEMPO Level 1B Radiance Product
https://dx.doi.org/10.5067/IS-40e/TEMPO/CLDO4_L2.003	TEMPO Level 2 Cloud Product

6.3. Output Data Access

URL	Description
https://doi.org/10.5067/IS-40e/TEMPO/NO2_L2.003	TEMPO Level 2 NO_2 Product
https://doi.org/10.5067/IS-40e/TEMPO/NO2_L3.003	TEMPO Level 3 (gridded) NO_2 Product

6.4. Important Related URLs

URL	Description
https://tempo.si.edu	Smithsonian Institution project homepage
https://asdc.larc.nasa.gov/project/TEMPO	ASDC project homepage

Contact Details

Caroline Nowlan	
Roles	Writing – original draft & Writing – review & editing & Corresponding Author
Affiliation	Center for Astrophysics | Harvard & Smithsonian
Email	cnowlan@cfa.harvard.edu
URL	https://www.cfa.harvard.edu/people/caroline-nowlan
UUID	https://orcid.org/0000-0002-8718-9752

Gonzalo González Abad	
Roles	Writing – original draft, Writing – review & editing
Affiliation	Center for Astrophysics | Harvard & Smithsonian
Email	ggonzalezabad@cfa.harvard.edu
URL	https://www.cfa.harvard.edu/people/gonzalo-gonzalez-abad
UUID	https://orcid.org/0000-0002-8090-6480

Xiong Liu	
Roles	Writing – original draft, Writing – review & editing & Funding acquisition
Affiliation	Center for Astrophysics | Harvard & Smithsonian
Email	xliu@cfa.harvard.edu
URL	https://lweb.cfa.harvard.edu/~xliu/
UUID	http://orcid.org/0000-0003-2939-574X

Huiqun Wang	
Roles	Writing – review & editing
Affiliation	Center for Astrophysics | Harvard & Smithsonian
Email	hwang@cfa.harvard.edu
URL	https://lweb.cfa.harvard.edu/~hwang/
UUID	https://orcid.org/0000-0001-9722-9992

References

Aliwell, S. R., Van Roozendael, M., Johnston, P. V., Richter, A., Wagner, T., Arlander, D. W., Burrows, J. P., Fish, D. J., Jones, R. L., Tørnkvist, K. K., Lambert, J. -C., Pfeilsticker, K., & Pundt, I. (2002). Analysis for BrO in zenith-sky spectra: An intercomparison exercise for analysis improvement. *Journal of Geophysical Research: Atmospheres*, *107*(D14). https://doi.org/10.1029/2001JD000329

Bak, J., Liu, X., Kim, J. H., Haffner, D. P., Chance, K., Yang, K., & Sun, K. (2017). Characterization and correction of OMPS nadir mapper measurements for ozone profile retrievals. *Atmospheric Measurement Techniques*, *10*(11), 4373–4388. https://doi.org/10.5194/amt-10-4373-2017

Beirle, S., Lampel, J., Lerot, C., Sihler, H., & Wagner, T. (2017). Parameterizing the instrumental spectral response function and its changes by a super-Gaussian and its derivatives. *Atmospheric Measurement Techniques*, *10*(2), 581–598. https://doi.org/10.5194/amt-10-581-2017

Bey, I., Jacob, D. J., Yantosca, R. M., Logan, J. A., Field, B. D., Fiore, A. M., Li, Q.-B., Liu, H. Y., Mickley, L. J., & Schultz, M. G. (2001). Global modeling of tropospheric chemistry with assimilated meteorology: Model description and evaluation. *Journal of Geophysical Research: Atmospheres*, *106*(D19), 23073–23095. https://doi.org/10.1029/2001JD000807

Bobbink, R., Hicks, K., Galloway, J., Spranger, T., Alkemade, R., Ashmore, M., Bustamante, M., Cinderby, S., Davidson, E., Dentener, F., Emmett, B., Erisman, J.-W., Fenn, M., Gilliam, F., Nordin, A., Pardo, L., & De Vries, W. (2010). Global assessment of nitrogen deposition effects on terrestrial plant diversity: A synthesis. *Ecological Applications*, *20*(1), 30–59. https://doi.org/10.1890/08-1140.1

Boersma, K. F., Eskes, H. J., & Brinksma, E. J. (2004). Error analysis for tropospheric NO_2 retrieval from space. *Journal of Geophysical Research: Atmospheres*, *109*(D4), 2003JD003962. https://doi.org/10.1029/2003JD003962

Boersma, K. F., Eskes, H. J., Dirksen, R. J., van der A, R. J., Veefkind, J. P., Stammes, P., Huijnen, V., Kleipool, Q. L., Sneep, M., Claas, J., Leitão, J., Richter, A., Zhou, Y., & Brunner, D. (2011). An improved tropospheric NO_2 column retrieval algorithm for the Ozone Monitoring Instrument. *Atmospheric Measurement Techniques*, *4*(9), 1905–1928. https://doi.org/10.5194/amt-4-1905-2011

Boersma, K. F., Eskes, H. J., Richter, A., De Smedt, I., Lorente, A., Beirle, S., Van Geffen, J. H. G. M., Zara, M., Peters, E., Van Roozendael, M., Wagner, T., Maasakkers, J. D., Van Der A, R. J., Nightingale, J., De Rudder, A., Irie, H., Pinardi, G., Lambert, J.-C., & Compernolle, S. C. (2018). Improving algorithms and uncertainty estimates for satellite NO_2 retrievals: Results from the quality assurance for the essential climate variables (QA4ECV) project. *Atmospheric Measurement Techniques*, *11*(12), 6651–6678. https://doi.org/10.5194/amt-11-6651-2018

Boersma, K. F., Jacob, D. J., Eskes, H. J., Pinder, R. W., Wang, J., & van der A, R. J. (2008). Intercomparison of SCIAMACHY and OMI tropospheric NO_2 columns: Observing the diurnal evolution of chemistry and emissions from space. *Journal of Geophysical Research*, *113*(D16), D16S26. https://doi.org/10.1029/2007JD008816

Bovensmann, H., Burrows, J. P., Buchwitz, M., Frerick, J., Noël, S., Rozanov, V. V., Chance, K. V., & Goede, A. P. H. (1999). SCIAMACHY: Mission Objectives and Measurement Modes. *Journal of the Atmospheric Sciences*, *56*(2), 127–150. https://doi.org/10.1175/1520-0469(1999)056<0127:SMOAMM>2.0.CO;2

Bucsela, E. J., Krotkov, N. A., Celarier, E. A., Lamsal, L. N., Swartz, W. H., Bhartia, P. K., Boersma, K. F., Veefkind, J. P., Gleason, J. F., & Pickering, K. E. (2013). A new stratospheric and tropospheric NO_2 retrieval algorithm for nadir-viewing satellite instruments: Applications to OMI. *Atmospheric Measurement Techniques*, *6*(10), 2607–2626. https://doi.org/10.5194/amt-6-2607-2013

Burnett, R., Chen, H., Szyszkowicz, M., Fann, N., Hubbell, B., Pope, C. A., Apte, J. S., Brauer, M., Cohen, A., Weichenthal, S., Coggins, J., Di, Q., Brunekreef, B., Frostad, J., Lim, S. S., Kan, H., Walker, K. D., Thurston, G. D., Hayes, R. B., … Spadaro, J. V. (2018). Global estimates of mortality associated with long-term exposure to outdoor fine particulate matter. *Proceedings of the National Academy of Sciences*, *115*(38), 9592–9597. https://doi.org/10.1073/pnas.1803222115

Burrows, J. P., Weber, M., Buchwitz, M., Rozanov, V., Ladstätter-Weißenmayer, A., Richter, A., DeBeek, R., Hoogen, R., Bramstedt, K., Eichmann, K.-U., Eisinger, M., & Perner, D. (1999). The Global Ozone Monitoring Experiment (GOME): Mission Concept and First Scientific Results. *Journal of the Atmospheric Sciences*, *56*(2), 151–175. https://doi.org/10.1175/1520-0469(1999)056<0151:TGOMEG>2.0.CO;2

Carn, S. (2019). *Multi-Satellite Volcanic Sulfur Dioxide L4 Long-Term Global Database V3* [Dataset]. NASA Goddard Earth Sciences Data and Information Services Center. https://doi.org/10.5067/MEASURES/SO2/DATA404

Castellanos, P., Boersma, K. F., Torres, O., & De Haan, J. F. (2015). OMI tropospheric NO_2 air mass factors over South America: Effects of biomass burning aerosols. *Atmospheric Measurement Techniques*, *8*(9), 3831–3849. https://doi.org/10.5194/amt-8-3831-2015

Chan Miller, C., Gonzalez Abad, G., Wang, H., Liu, X., Kurosu, T., Jacob, D. J., & Chance, K. (2014). Glyoxal retrieval from the Ozone Monitoring Instrument. *Atmospheric Measurement Techniques*, *7*(11), 3891–3907. https://doi.org/10.5194/amt-7-3891-2014

Chan Miller, C., Nowlan, C. R., Bak, J., Liu, X., Gonzalez Abad, G., Zoogman, P., & Chance, K. (2019). *A probabilistic model of surface reflectance for atmospheric retrieval algorithms from the UV to SWIR*. *2019*, A13J-2935. AGU Fall Meeting Abstracts.

Chance, K., Kurosu, T. P., & Sioris, C. E. (2005). Undersampling correction for array detector-based satellite spectrometers. *Applied Optics*, *44*(7), 1296. https://doi.org/10.1364/AO.44.001296

Chance, K., Palmer, P., & Spurr, R. (2000). Satellite observations of formaldehyde over North America. *Geophysical Research Letters*, *27*(21), 3461–3464.

Chance, K., & Spurr, R. J. D. (1997). Ring effect studies: Rayleigh scattering, including molecular parameters for rotational Raman scattering, and the Fraunhofer spectrum. *Applied Optics*, *36*(21), 5224. https://doi.org/10.1364/ao.36.005224

Chong, H., Liu, X., Houck, J. C., Flittner, D. E., Carr, J., Hou, W., Davis, J. E., Suleiman, R. M., Chance, K., & Mishra, N. (2025). *Algorithm theoretical basis document for the TEMPO Level 0-1 processor*.

Coddington, O. M., Richard, E. C., Harber, D., Pilewskie, P., Woods, T. N., Snow, M., Chance, K., Liu, X., & Sun, K. (2023). Version 2 of the TSIS-1 Hybrid Solar Reference Spectrum and Extension to the Full Spectrum. *Earth and Space Science*, *10*(3), e2022EA002637. https://doi.org/10.1029/2022EA002637

Cox, C., & Munk, W. (1954). Measurement of the Roughness of the Sea Surface from Photographs of the Sun's Glitter. *Journal of the Optical Society of America*, *44*(11), 838. https://doi.org/10.1364/JOSA.44.000838

Danielson, J. J., & Gesch, D. B. (2011). Global Multi-Resolution Terrain Elevation Data 2010 (GMTED2010). *US Geological Survey Open-File Report*.

Darmenov, A., & da Silva, A. (2015). *The Quick Fire Emissions Dataset (QFED)—Documentation of versions 2.1, 2.2 and 2.4* (38; Technical Report Series on Global Modeling and Data Assimilation, p. 212).

Eastham, S. D., Weisenstein, D. K., & Barrett, S. R. H. (2014). Development and evaluation of the unified tropospheric–stratospheric chemistry extension (UCX) for the global chemistry-transport model GEOS-Chem. *Atmospheric Environment*, *89*, 52–63. https://doi.org/10.1016/j.atmosenv.2014.02.001

Fasnacht, Z., Vasilkov, A., Haffner, D., Qin, W., Joiner, J., Krotkov, N., Sayer, A. M., & Spurr, R. (2019). A geometry-dependent surface Lambertian-equivalent reflectivity product for UV-Vis

retrievals—Part 2: Evaluation over open ocean. *Atmospheric Measurement Techniques*, *12*(12), 6749–6769. https://doi.org/10.5194/amt-12-6749-2019

Finkenzeller, H., & Volkamer, R. (2022). O_2–O_2 CIA in the gas phase: Cross-section of weak bands, and continuum absorption between 297–500 nm. *Journal of Quantitative Spectroscopy and Radiative Transfer*, *279*, 108063. https://doi.org/10.1016/j.jqsrt.2021.108063

Fiore, A. M., Mickley, L. J., Zhu, Q., & Baublitz, C. B. (2024). Climate and Tropospheric Oxidizing Capacity. *Annual Review of Earth and Planetary Sciences*, *52*(1), 321–349. https://doi.org/10.1146/annurev-earth-032320-090307

Fishman, J., Iraci, L. T., Al-Saadi, J., Chance, K., Chavez, F., Chin, M., Coble, P., Davis, C., DiGiacomo, P. M., Edwards, D., Eldering, A., Goes, J., Herman, J., Hu, C., Jacob, D. J., Jordan, C., Kawa, S. R., Key, R., Liu, X., … Wang, M. (2012). The United States' next generation of atmospheric composition and coastal ecosystem measurements: NASA's geostationary coastal and air pollution events (GEO-CAPE) mission. *Bulletin of the American Meteorological Society*, *93*(10), 1547–1566. https://doi.org/10.1175/BAMS-D-11-00201.1

Flynn, L., Long, C., Wu, X., Evans, R., Beck, C. T., Petropavlovskikh, I., McConville, G., Yu, W., Zhang, Z., Niu, J., Beach, E., Hao, Y., Pan, C., Sen, B., Novicki, M., Zhou, S., & Seftor, C. (2014). Performance of the Ozone Mapping and Profiler Suite (OMPS) products. *Journal of Geophysical Research: Atmospheres*, *119*, 6181–6195. https://doi.org/10.1002/2013JD020467

Geddes, J. A., Martin, R. V., Bucsela, E. J., McLinden, C. A., & Cunningham, D. J. M. (2018). Stratosphere-troposphere separation of nitrogen dioxide columns from the TEMPO geostationary satellite instrument. *Atmospheric Measurement Techniques*, *11*(11), 6271–6287. https://doi.org/10.5194/amt-11-6271-2018

Gelaro, R., McCarty, W., Suárez, M. J., Todling, R., Molod, A., Takacs, L., Randles, C. A., Darmenov, A., Bosilovich, M. G., Reichle, R., Wargan, K., Coy, L., Cullather, R., Draper, C., Akella, S., Buchard, V., Conaty, A., da Silva, A. M., Gu, W., … Zhao, B. (2017). The Modern-Era Retrospective Analysis for Research and Applications, Version 2 (MERRA-2). *Journal of Climate*, *30*(14), 5419–5454. https://doi.org/10.1175/JCLI-D-16-0758.1

González Abad, G., Liu, X., Chance, K., Wang, H., Kurosu, T. P., & Suleiman, R. (2015). Updated Smithsonian Astrophysical Observatory Ozone Monitoring Instrument (SAO OMI) formaldehyde retrieval. *Atmospheric Measurement Techniques*, *8*(1), 19–32. https://doi.org/10.5194/amt-8-19-2015

González Abad, G., Nowlan, C. R., Wang, H., Chong, H., Houck, J., Liu, X., & Chance, K. (2024). *TEMPO Trace Gas and Cloud Level 2 and 3 Data Products: User Guide*. https://asdc.larc.nasa.gov/documents/tempo/guide/TEMPO_Level-2-3_trace_gas_clouds_user_guide_V1.2.pdf

González Abad, G., Souri, A. H., Bak, J., Chance, K., Flynn, L. E., Krotkov, N. A., Lamsal, L., Li, C., Liu, X., Miller, C. C., Nowlan, C. R., Suleiman, R., & Wang, H. (2019). Five decades observing Earth's atmospheric trace gases using ultraviolet and visible backscatter solar radiation from space. *Journal of Quantitative Spectroscopy and Radiative Transfer*. https://doi.org/10.1016/j.jqsrt.2019.04.030

González Abad, G., Vasilkov, A., Seftor, C., Liu, X., & Chance, K. (2016). Smithsonian Astrophysical Observatory Ozone Mapping and Profiler Suite (SAO OMPS) formaldehyde retrieval. *Atmospheric Measurement Techniques*, *9*(7), 2797–2812. https://doi.org/10.5194/amt-9-2797-2016

Gordon, I. E., Rothman, L. S., Hargreaves, R. J., Hashemi, R., Karlovets, E. V., Skinner, F. M., Conway, E. K., Hill, C., Kochanov, R. V., Tan, Y., Wcisło, P., Finenko, A. A., Nelson, K., Bernath, P. F., Birk, M., Boudon, V., Campargue, A., Chance, K. V., Coustenis, A., … Yurchenko, S. N. (2022). The HITRAN2020 molecular spectroscopic database. *Journal of Quantitative Spectroscopy and Radiative Transfer*, *277*, 107949. https://doi.org/10.1016/j.jqsrt.2021.107949

Griffin, D., McLinden, C. A., Dammers, E., Adams, C., Stockwell, C. E., Warneke, C., Bourgeois, I., Peischl, J., Ryerson, T. B., Zarzana, K. J., Rowe, J. P., Volkamer, R., Knote, C., Kille, N.,

Koenig, T. K., Lee, C. F., Rollins, D., Rickly, P. S., Chen, J., … Makar, P. (2021). Biomass burning nitrogen dioxide emissions derived from space with TROPOMI: Methodology and validation. *Atmospheric Measurement Techniques*, *14*(12), 7929–7957. https://doi.org/10.5194/amt-14-7929-2021

Guenther, A. B., Jiang, X., Heald, C. L., Sakulyanontvittaya, T., Duhl, T., Emmons, L. K., & Wang, X. (2012). The Model of Emissions of Gases and Aerosols from Nature version 2.1 (MEGAN2.1): An extended and updated framework for modeling biogenic emissions. *Geoscientific Model Development*, *5*(6), 1471–1492. https://doi.org/10.5194/gmd-5-1471-2012

Helfrich, S., Li, M., Kongoli, C., Nagdimunov, L., & Rodriguez, E. (2018). *Interactive Multisensor Snow and Ice Mapping System Version 3 (IMS V3) ATBD Version 2.5* (p. 74). NOAA NESDIC STAR.

Huang, X., Yang, K., Kondragunta, S., Wei, Z., Valin, L., Szykman, J., & Goldberg, M. (2022). NO_2 retrievals from NOAA-20 OMPS: Algorithm, evaluation, and observations of drastic changes during COVID-19. *Atmospheric Environment*, *290*, 119367. https://doi.org/10.1016/j.atmosenv.2022.119367

Hudman, R. C., Moore, N. E., Mebust, a. K., Martin, R. V., Russell, a. R., Valin, L. C., & Cohen, R. C. (2012). Steps towards a mechanistic model of global soil nitric oxide emissions: Implementation and space based-constraints. *Atmospheric Chemistry and Physics*, *12*(16), 7779–7795. https://doi.org/10.5194/acp-12-7779-2012

IPCC. (2023a). Global Carbon and other Biogeochemical Cycles and Feedbacks. In *Climate Change 2021 – The Physical Science Basis: Working Group I Contribution to the Sixth Assessment Report of the Intergovernmental Panel on Climate Change* (1st ed., pp. 673–816). Cambridge University Press. https://doi.org/10.1017/9781009157896

IPCC. (2023b). Short-lived Climate Forcers. In *Climate Change 2021 – The Physical Science Basis: Working Group I Contribution to the Sixth Assessment Report of the Intergovernmental Panel on Climate Change* (1st ed., pp. 817–922). Cambridge University Press. https://doi.org/10.1017/9781009157896

Jacob, D. J. (2000). *Introduction to Atmospheric Chemistry*. Princeton University Press.

Janssens-Maenhout, G., Crippa, M., Guizzardi, D., Dentener, F., Muntean, M., Pouliot, G., Keating, T., Zhang, Q., Kurokawa, J., Wankmüller, R., Denier Van Der Gon, H., Kuenen, J. J. P., Klimont, Z., Frost, G., Darras, S., Koffi, B., & Li, M. (2015). HTAP_v2.2: A mosaic of regional and global emission grid maps for 2008 and 2010 to study hemispheric transport of air pollution. *Atmospheric Chemistry and Physics*, *15*(19), 11411–11432. https://doi.org/10.5194/acp-15-11411-2015

Keller, C. A., Knowland, K. E., Duncan, B. N., Liu, J., Anderson, D. C., Das, S., Lucchesi, R. A., Lundgren, E. W., Nicely, J. M., Nielsen, E., Ott, L. E., Saunders, E., Strode, S. A., Wales, P. A., Jacob, D. J., & Pawson, S. (2021). Description of the NASA GEOS Composition Forecast Modeling System GEOS-CF v1.0. *Journal of Advances in Modeling Earth Systems*, *13*(4), 1–31. https://doi.org/10.1029/2020MS002413

Keller, C. A., Long, M. S., Yantosca, R. M., Da Silva, A. M., Pawson, S., & Jacob, D. J. (2014). HEMCO v1.0: A versatile, ESMF-compliant component for calculating emissions in atmospheric models. *Geoscientific Model Development*, *7*(4), 1409–1417. https://doi.org/10.5194/gmd-7-1409-2014

Kim, J., Jeong, U., Ahn, M. H., Kim, J. H., Park, R. J., Lee, H., Song, C. H., Choi, Y. S., Lee, K. H., Yoo, J. M., Jeong, M. J., Park, S. K., Lee, K. M., Song, C. K., Kim, S. W., Kim, Y. J., Kim, S. W., Kim, M., Go, S., … Choi, Y. (2020). New era of air quality monitoring from space: Geostationary environment monitoring spectrometer (GEMS). *Bulletin of the American Meteorological Society*, *101*(1), E1–E22. https://doi.org/10.1175/BAMS-D-18-0013.1

Knowland, K. E., Keller, C. A., & Lucchesi, R. (2022). *File Specification for GEOS-CF Products* (p. 54) [GMAO Office Note].

Knowland, K. E., Keller, C. A., Wales, P. A., Wargan, K., Coy, L., Johnson, M. S., Liu, J., Lucchesi, R. A., Eastham, S. D., Fleming, E., Liang, Q., Leblanc, T., Livesey, N. J., Walker, K. A., Ott, L. E., & Pawson, S. (2022). NASA GEOS Composition Forecast Modeling System GEOS-CF v1.0:

Stratospheric Composition. *Journal of Advances in Modeling Earth Systems*, *14*(6), e2021MS002852. https://doi.org/10.1029/2021MS002852

Kokaly, R. F., Clark, R. N., Swayze, G. A., Livo, K. E., Hoefen, T. M., Pearson, N. C., Wise, R. A., Benzel, W., Lowers, H. A., Driscoll, R. L., & Klein, A. J. (2017). *USGS Spectral Library Version 7* (1035; U.S. Geological Survey Data Series, p. 61). https://pubs.usgs.gov/publication/ds1035

Kwon, H.-A., González Abad, G., Chan Miller, C., Hall, K. R., Nowlan, C. R., O'Sullivan, E., Wang, H., Chong, H., Ayazpour, Z., Liu, X., & Chance, K. (2024). Updated OMI Glyoxal Column Measurements Using Collection 4 Level 1B Radiances. *Earth and Space Science*, *11*(9), e2024EA003705. https://doi.org/10.1029/2024EA003705

Kwon, H.-A., Park, R. J., González Abad, G., Chance, K., Kurosu, T. P., Kim, J., De Smedt, I., Van Roozendael, M., Peters, E., & Burrows, J. (2019). Description of a formaldehyde retrieval algorithm for the Geostationary Environment Monitoring Spectrometer (GEMS). *Atmospheric Measurement Techniques*, *12*(7), 3551–3571. https://doi.org/10.5194/amt-12-3551-2019

Lamsal, L. N., Krotkov, N. A., Vasilkov, A., Marchenko, S., Qin, W., Yang, E.-S., Fasnacht, Z., Joiner, J., Choi, S., Haffner, D., Swartz, W. H., Fisher, B., & Bucsela, E. (2021). Ozone Monitoring Instrument (OMI) Aura nitrogen dioxide standard product version 4.0 with improved surface and cloud treatments. *Atmospheric Measurement Techniques*, *14*(1), 455–479. https://doi.org/10.5194/amt-14-455-2021

Leitão, J., Richter, A., Vrekoussis, M., Kokhanovsky, A., Zhang, Q. J., Beekmann, M., & Burrows, J. P. (2010). On the improvement of NO_2 satellite retrievals—Aerosol impact on the airmass factors. *Atmospheric Measurement Techniques*, *3*(2), 475–493. https://doi.org/10.5194/amt-3-475-2010

Levelt, P. F., Oord, G. H. J. V. D., Dobber, M. R., Mälkki, A., Visser, H., Vries, J. D., Stammes, P., Lundell, J. O. V., & Saari, H. (2006). The Ozone Monitoring Instrument. *IEEE Trans. Geosci. Remote Sens.*, *44*(5), 1093–1101.

Liu, C., Liu, X., Kowalewski, M. G., Janz, S. J., González Abad, G., Pickering, K. E., Chance, K., & Lamsal, L. N. (2015). Characterization and verification of ACAM slit functions for trace-gas retrievals during the 2011 DISCOVER-AQ flight campaign. *Atmospheric Measurement Techniques*, *8*, 751–759. https://doi.org/10.5194/amt-8-751-2015

Liu, F., Choi, S., Li, C., Fioletov, V. E., McLinden, C. A., Joiner, J., Krotkov, N. A., Bian, H., Janssens-Maenhout, G., Darmenov, A. S., & da Silva, A. M. (2018). A new global anthropogenic SO_2 emission inventory for the last decade: A mosaic of satellite-derived and bottom-up emissions. *Atmospheric Chemistry and Physics*, *18*(22), 16571–16586. https://doi.org/10.5194/acp-18-16571-2018

Liu, S., Valks, P., Pinardi, G., De Smedt, I., Yu, H., Beirle, S., & Richter, A. (2019). An improved total and tropospheric NO_2 column retrieval for GOME-2. *Atmospheric Measurement Techniques*, *12*(2), 1029–1057. https://doi.org/10.5194/amt-12-1029-2019

Liu, X., Bhartia, P. K., Chance, K., Spurr, R. J. D., & Kurosu, T. P. (2010). Ozone profile retrievals from the Ozone Monitoring Instrument. *Atmospheric Chemistry and Physics*, *10*(5), 2521–2537. https://doi.org/10.5194/acp-10-2521-2010

Lorente, A., Folkert Boersma, K., Yu, H., Dörner, S., Hilboll, A., Richter, A., Liu, M., Lamsal, L. N., Barkley, M., De Smedt, I., Van Roozendael, M., Wang, Y., Wagner, T., Beirle, S., Lin, J.-T., Krotkov, N., Stammes, P., Wang, P., Eskes, H. J., & Krol, M. (2017). Structural uncertainty in air mass factor calculation for NO_2 and HCHO satellite retrievals. *Atmospheric Measurement Techniques*, *10*(3), 759–782. https://doi.org/10.5194/amt-10-759-2017

Lucchesi, R. (2015). *File Specification for GEOS-5 FP-IT (Forward Processing for Instrument Teams)* (p. 64) [GMAO Office Note].

Mao, J., Paulot, F., Jacob, D. J., Cohen, R. C., Crounse, J. D., Wennberg, P. O., Keller, C. A., Hudman, R. C., Barkley, M. P., & Horowitz, L. W. (2013). Ozone and organic nitrates over the eastern United States: Sensitivity to isoprene chemistry. *Journal of Geophysical Research: Atmospheres*, *118*(19). https://doi.org/10.1002/jgrd.50817

Marais, E. A., Jacob, D. J., Jimenez, J. L., Campuzano-Jost, P., Day, D. A., Hu, W., Krechmer, J., Zhu, L., Kim, P. S., Miller, C. C., Fisher, J. A., Travis, K., Yu, K., Hanisco, T. F., Wolfe, G. M., Arkinson, H. L., Pye, H. O. T., Froyd, K. D., Liao, J., & McNeill, V. F. (2016). Aqueous-phase mechanism for secondary organic aerosol formation from isoprene: Application to the southeast United States and co-benefit of SO_2 emission controls. *Atmospheric Chemistry and Physics*, *16*(3), 1603–1618. https://doi.org/10.5194/acp-16-1603-2016

Martin, R., Chance, K., Jacob, D., Kuroru, T., Spurr, R., Bucsela, E., Gleason, J., Palmer, P., Bey, I., Fiore, A., Li, Q., Yantosca, R., & Koelemeijer, R. (2002). An improved retrieval of tropospheric nitrogen dioxide from GOME. *Journal of Geophysical Research*, *107*(D20), 4437. https://doi.org/10.1029/2001JD001027

Mason, J. D., Cone, M. T., & Fry, E. S. (2016). Ultraviolet (250–550 nm) absorption spectrum of pure water. *Applied Optics*, *55*(25), 7163. https://doi.org/10.1364/AO.55.007163

Munro, R., Lang, R., Klaes, D., Poli, G., Retscher, C., Lindstrot, R., Huckle, R., Lacan, A., Grzegorski, M., Holdak, A., Kokhanovsky, A., Livschitz, J., & Eisinger, M. (2016). The GOME-2 instrument on the Metop series of satellites: Instrument design, calibration, and level 1 data processing—An overview. *Atmospheric Measurement Techniques*, *9*(3), 1279–1301. https://doi.org/10.5194/amt-9-1279-2016

Murray, L. T., Jacob, D. J., Logan, J. A., Hudman, R. C., & Koshak, W. J. (2012). Optimized regional and interannual variability of lightning in a global chemical transport model constrained by LIS/OTD satellite data. *Journal of Geophysical Research: Atmospheres*, *117*(D20), 2012JD017934. https://doi.org/10.1029/2012JD017934

Noël, S., Bramstedt, K., Bovensmann, H., Gerilowski, K., Burrows, J. P., Standfuss, C., Dufour, E., & Veihelmann, B. (2012). Quantification and mitigation of the impact of scene inhomogeneity on Sentinel-4 UVN UV-VIS retrievals. *Atmospheric Measurement Techniques*, *5*(6), 1319–1331. https://doi.org/10.5194/amt-5-1319-2012

Nowlan, C. R., González Abad, G., Kwon, H. -A., Ayazpour, Z., Chan Miller, C., Chance, K., Chong, H., Liu, X., O'Sullivan, E., Wang, H., Zhu, L., De Smedt, I., Jaross, G., Seftor, C., & Sun, K. (2023). Global formaldehyde products from the Ozone Mapping and Profiler Suite (OMPS) Nadir Mappers on Suomi NPP and NOAA-20. *Earth and Space Science*, *10*(5). https://doi.org/10.1029/2022EA002643

Nowlan, C. R., Liu, X., Chance, K., Cai, Z., Kurosu, T. P., Lee, C., & Martin, R. V. (2011). Retrievals of sulfur dioxide from the Global Ozone Monitoring Experiment 2 (GOME-2) using an optimal estimation approach: Algorithm and initial validation. *Journal of Geophysical Research*, *116*(D18), D18301. https://doi.org/10.1029/2011JD015808

Nowlan, C. R., Liu, X., Janz, S. J., Kowalewski, M. G., Chance, K., Follette-Cook, M. B., Fried, A., González Abad, G., Herman, J. R., Judd, L. M., Kwon, H.-A., Loughner, C. P., Pickering, K. E., Richter, D., Spinei, E., Walega, J., Weibring, P., & Weinheimer, A. J. (2018). Nitrogen dioxide and formaldehyde measurements from the GEOstationary Coastal and Air Pollution Events (GEO-CAPE) Airborne Simulator over Houston, Texas. *Atmospheric Measurement Techniques*, *11*(11), 5941–5964. https://doi.org/10.5194/amt-11-5941-2018

Nowlan, C. R., Liu, X., Leitch, J. W., Chance, K., González Abad, G., Liu, C., Zoogman, P., Cole, J., Delker, T., Good, W., Murcray, F., Ruppert, L., Soo, D., Follette-Cook, M. B., Janz, S. J., Kowalewski, M. G., Loughner, C. P., Pickering, K. E., Herman, J. R., … Al-Saadi, J. A. (2016). Nitrogen dioxide observations from the Geostationary Trace gas and Aerosol Sensor Optimization (GeoTASO) airborne instrument: Retrieval algorithm and measurements during DISCOVER-AQ Texas 2013. *Atmospheric Measurement Techniques*, *9*(6), 2647–2668. https://doi.org/10.5194/amt-9-2647-2016

Oda, T., Maksyutov, S., & Andres, R. J. (2018). The Open-source Data Inventory for Anthropogenic CO_2, version 2016 (ODIAC2016): A global monthly fossil fuel CO_2 gridded emissions data product for tracer transport simulations and surface flux inversions. *Earth System Science Data*, *10*(1), 87–107. https://doi.org/10.5194/essd-10-87-2018

Palmer, P. I., Jacob, D. J., Chance, K., Martin, R. V., Spurr, R. J. D., Kurosu, T. P., Bey, I., Yantosca, R., Fiore, A., & Li, Q. (2001). Air mass factor formulation for spectroscopic measurements from satellites: Application to formaldehyde retrievals from the Global Ozone Monitoring Experiment. *Journal of Geophysical Research: Atmospheres*, *106*(D13), 14539–14550. https://doi.org/10.1029/2000JD900772

Parrella, J. P., Chance, K., Salawitch, R. J., Canty, T., Dorf, M., & Pfeilsticker, K. (2013). New retrieval of BrO from SCIAMACHY limb: An estimate of the stratospheric bromine loading during April 2008. *Atmospheric Measurement Techniques*, *6*(10), 2549–2561. https://doi.org/10.5194/amt-6-2549-2013

Parrella, J. P., Jacob, D. J., Liang, Q., Zhang, Y., Mickley, L. J., Miller, B., Evans, M. J., Yang, X., Pyle, J. A., Theys, N., & Van Roozendael, M. (2012). Tropospheric bromine chemistry: Implications for present and pre-industrial ozone and mercury. *Atmospheric Chemistry and Physics*, *12*(15), 6723–6740. https://doi.org/10.5194/acp-12-6723-2012

Peng, S., Lin, X., Thompson, R. L., Xi, Y., Liu, G., Hauglustaine, D., Lan, X., Poulter, B., Ramonet, M., Saunois, M., Yin, Y., Zhang, Z., Zheng, B., & Ciais, P. (2022). Wetland emission and atmospheric sink changes explain methane growth in 2020. *Nature*, *612*(7940), 477–482. https://doi.org/10.1038/s41586-022-05447-w

Prather, M. J., Hsu, J., DeLuca, N. M., Jackman, C. H., Oman, L. D., Douglass, A. R., Fleming, E. L., Strahan, S. E., Steenrod, S. D., Søvde, O. A., Isaksen, I. S. A., Froidevaux, L., & Funke, B. (2015). Measuring and modeling the lifetime of nitrous oxide including its variability. *Journal of Geophysical Research: Atmospheres*, *120*(11), 5693–5705. https://doi.org/10.1002/2015JD023267

Qin, W., Fasnacht, Z., Haffner, D., Vasilkov, A., Joiner, J., Krotkov, N., Fisher, B., & Spurr, R. (2019). A geometry-dependent surface Lambertian-equivalent reflectivity product for UV-Vis retrievals—Part 1: Evaluation over land surfaces using measurements from OMI at 466 nm. *Atmospheric Measurement Techniques*, *12*(7), 3997–4017. https://doi.org/10.5194/amt-12-3997-2019

Richter, A., Begoin, M., Hilboll, A., & Burrows, J. P. (2011). An improved NO_2 retrieval for the GOME-2 satellite instrument. *Atmospheric Measurement Techniques*, *4*(6), 1147–1159. https://doi.org/10.5194/amt-4-1147-2011

Richter, A., & Burrows, J. P. (2002). Tropospheric NO_2 from GOME measurements. *Advances in Space Research*, *29*(11), 1673–1683. https://doi.org/10.1016/S0273-1177(02)00100-X

Schaaf, C., & Wang, Z. (2015a). *MCD43C1 MODIS/Terra+Aqua BRDF/AlbedoModel Parameters Daily L3 Global 0.05Deg CMG V006* [Dataset]. NASA EOSDIS Land Processes Distributed Active Archive Center. https://doi.org/10.5067/MODIS/MCD43C1.006

Schaaf, C., & Wang, Z. (2015b). *MCD43C2 MODIS/Terra+Aqua BRDF/Albedo Snow-free Model Parameters Daily L3 Global 0.05Deg CMG V006* [Dataset]. NASA EOSDIS Land Processes Distributed Active Archive Center. https://doi.org/10.5067/MODIS/MCD43C2.006

Schultz, M. G., Heil, A., Hoelzemann, J. J., Spessa, A., Thonicke, K., Goldammer, J. G., Held, A. C., Pereira, J. M. C., & Van Het Bolscher, M. (2008). Global wildland fire emissions from 1960 to 2000. *Global Biogeochemical Cycles*, *22*(2), 2007GB003031. https://doi.org/10.1029/2007GB003031

Serdyuchenko, A., Gorshelev, V., Weber, M., Chehade, W., & Burrows, J. P. (2014). High spectral resolution ozone absorption cross-sections—Part 2: Temperature dependence. *Atmospheric Measurement Techniques*, *7*(2), 625–636. https://doi.org/10.5194/amt-7-625-2014

Sherwen, T., Schmidt, J. A., Evans, M. J., Carpenter, L. J., Großmann, K., Eastham, S. D., Jacob, D. J., Dix, B., Koenig, T. K., Sinreich, R., Ortega, I., Volkamer, R., Saiz-Lopez, A., Prados-Roman, C., Mahajan, A. S., & Ordóñez, C. (2016). Global impacts of tropospheric halogens (Cl, Br, I) on oxidants and composition in GEOS-Chem. *Atmospheric Chemistry and Physics*, *16*(18), 12239–12271. https://doi.org/10.5194/acp-16-12239-2016

Sioris, C. E., Kurosu, T. P., Martin, R. V., & Chance, K. (2004). Stratospheric and tropospheric NO_2 observed by SCIAMACHY: first results. *Advances in Space Research*, *34*(4), 780–785. https://doi.org/10.1016/j.asr.2003.08.066

Spurr, R. J. D. (2006). VLIDORT: A linearized pseudo-spherical vector discrete ordinate radiative transfer code for forward model and retrieval studies in multilayer multiple scattering media. *Journal of Quantitative Spectroscopy and Radiative Transfer*, *102*(2), 316–342. https://doi.org/10.1016/j.jqsrt.2006.05.005

Suleiman, R. M., Chance, K., Liu, X., González Abad, G., Kurosu, T. P., Hendrick, F., & Theys, N. (2019). OMI total bromine monoxide (OMBRO) data product: Algorithm, retrieval and measurement comparisons. *Atmospheric Measurement Techniques*, *12*(4), 2067–2084. https://doi.org/10.5194/amt-12-2067-2019

Sun, K., Liu, X., Huang, G., González Abad, G., Cai, Z., Chance, K., & Yang, K. (2017). Deriving the slit functions from OMI solar observations and its implications for ozone-profile retrieval. *Atmospheric Measurement Techniques*, *10*(10), 3677–3695. https://doi.org/10.5194/amt-10-3677-2017

TEMPO Validation Team. (2023). *TEMPO Level 2 Science Data Product Validation Plan*.

TEMPO Validation Team. (2025). *Validation and Quality Assessment of the TEMPO Level-2 Trace Gas Products*.

Tilstra, L. G., Tuinder, O. N. E., Wang, P., & Stammes, P. (2017). Surface reflectivity climatologies from UV to NIR determined from Earth observations by GOME-2 and SCIAMACHY. *Journal of Geophysical Research: Atmospheres*, *122*(7), 4084–4111. https://doi.org/10.1002/2016JD025940

U.S. EPA. (2016). *Integrated Science Assessment (ISA) for Oxides of Nitrogen – Health Criteria (Final Report, Jan 2016)* (EPA/600/R-15/068). U.S. Environmental Protection Agency.

U.S. EPA. (2020). *Integrated Science Assessment (ISA) for Ozone and Related Photochemical Oxidants (Final Report, Apr 2020)* (EPA/600/R-20/012). U.S. Environmental Protection Agency.

van der Gon, H. D., Hendriks, C., Kuenen, J., Segers, A., & Visschedijk, A. (2011). *Description of current temporal emission patterns and sensitivity of predicted AQ for temporal emission patterns*. TNO.

van Geffen, J., Eskes, H., Compernolle, S., Pinardi, G., Verhoelst, T., Lambert, J.-C., Sneep, M., ter Linden, M., Ludewig, A., Boersma, K. F., & Veefkind, J. P. (2022). Sentinel-5P TROPOMI NO_2 retrieval: Impact of version v2.2 improvements and comparisons with OMI and ground-based data. *Atmospheric Measurement Techniques*, *15*(7), 2037–2060. https://doi.org/10.5194/amt-15-2037-2022

van Geffen, J., Eskes, H. J., Boersma, K. F., & Veefkind, J. P. (2022). *TROPOMI ATBD of the total and tropospheric NO_2 data products, issue 2.4.0* (S5P-KNMI-L2-0005-RP; p. 88). https://sentinel.esa.int/documents/247904/2476257/sentinel-5p-tropomi-atbd-no2-data-products

Vandaele, A. C., Hermans, C., Simon, P. C., Carleer, M., Colin, R., Fally, S., Mérienne, M. F., Jenouvrier, A., & Coquart, B. (1998). Measurements of the NO_2 absorption cross-section from 42 000 cm^{-1} to 10 000 cm^{-1} (238–1000 nm) at 220 K and 294 K. *Journal of Quantitative Spectroscopy and Radiative Transfer*, *59*(3–5), 171–184. https://doi.org/10.1016/S0022-4073(97)00168-4

Veefkind, J. P., Aben, I., McMullan, K., Förster, H., de Vries, J., Otter, G., Claas, J., Eskes, H. J., de Haan, J. F., Kleipool, Q., van Weele, M., Hasekamp, O., Hoogeveen, R., Landgraf, J., Snel, R., Tol, P., Ingmann, P., Voors, R., Kruizinga, B., … Levelt, P. F. (2012). TROPOMI on the ESA Sentinel-5 Precursor: A GMES mission for global observations of the atmospheric composition for climate, air quality and ozone layer applications. *Remote Sensing of Environment*, *120*(2012), 70–83. https://doi.org/10.1016/j.rse.2011.09.027

Voors, R., Dobber, M., Dirksen, R., & Levelt, P. (2006). Method of calibration to correct for cloud-induced wavelength shifts in the Aura satellite's Ozone Monitoring Instrument. *Applied Optics*, *45*(15), 3652. https://doi.org/10.1364/AO.45.003652

Wang, H., Nowlan, C. R., González Abad, G., Chong, H., Hou, W., Houck, J. C., Liu, X., Chance, K., Yang, E.-S., Vasilkov, A., Joiner, J., Qin, W., Fasnacht, Z., Knowland, K. E., Chan Miller, C., Spurr, R. J. D., Flittner, D., Carr, J. L., Suleiman, R., … Fitzmaurice, J. (2025). Algorithm theoretical basis for Version 3 TEMPO O_2-O_2 cloud product. *Earth and Space Science*, *12*, e2024EA004165.

Wang, H., Souri, A. H., González Abad, G., Liu, X., & Chance, K. (2019). Ozone Monitoring Instrument (OMI) Total Column Water Vapor version 4 validation and applications. *Atmospheric Measurement Techniques*, *12*(9), 5183–5199. https://doi.org/10.5194/amt-12-5183-2019

Wargan, K., Pawson, S., Olsen, M. A., Witte, J. C., Douglass, A. R., Ziemke, J. R., Strahan, S. E., & Nielsen, J. E. (2015). The global structure of upper troposphere-lower stratosphere ozone in GEOS-5: A multiyear assimilation of EOS Aura data. *Journal of Geophysical Research: Atmospheres*, *120*(5), 2013–2036. https://doi.org/10.1002/2014JD022493

Yang, K., Carn, S. A., Ge, C., Wang, J., & Dickerson, R. R. (2014). Advancing measurements of tropospheric NO_2 from space: New algorithm and first global results from OMPS. *Geophysical Research Letters*, *41*(13), 4777–4786. https://doi.org/10.1002/2014GL060136

Zara, M., Boersma, K. F., De Smedt, I., Richter, A., Peters, E., Van Geffen, J. H. G. M., Beirle, S., Wagner, T., Van Roozendael, M., Marchenko, S., Lamsal, L. N., & Eskes, H. J. (2018). Improved slant column density retrieval of nitrogen dioxide and formaldehyde for OMI and GOME-2A from QA4ECV: Intercomparison, uncertainty characterisation, and trends. *Atmospheric Measurement Techniques*, *11*(7), 4033–4058. https://doi.org/10.5194/amt-11-4033-2018

Zhang, C., Liu, C., Chan, K. L., Hu, Q., Liu, H., Li, B., Xing, C., Tan, W., Zhou, H., Si, F., & Liu, J. (2020). First observation of tropospheric nitrogen dioxide from the Environmental Trace Gases Monitoring Instrument onboard the GaoFen-5 satellite. *Light: Science & Applications*, *9*(1), 66. https://doi.org/10.1038/s41377-020-0306-z

Zhou, Y., Brunner, D., Boersma, K. F., Dirksen, R., & Wang, P. (2009). An improved tropospheric NO_2 retrieval for OMI observations in the vicinity of mountainous terrain. *Atmospheric Measurement Techniques*, *2*(2), 401–416. https://doi.org/10.5194/amt-2-401-2009

Zoogman, P., Liu, X., Chance, K., Sun, Q., Schaaf, C., Mahr, T., & Wagner, T. (2016). A climatology of visible surface reflectance spectra. *Journal of Quantitative Spectroscopy and Radiative Transfer*, *180*, 39–46. https://doi.org/10.1016/j.jqsrt.2016.04.003

Zoogman, P., Liu, X., Suleiman, R. M., Pennington, W. F., Flittner, D. E., Al-Saadi, J. A., Hilton, B. B., Nicks, D. K., Newchurch, M. J., Carr, J. L., Janz, S. J., Andraschko, M. R., Arola, A., Baker, B. D., Canova, B. P., Chan Miller, C., Cohen, R. C., Davis, J. E., Dussault, M. E., … Chance, K. (2017). Tropospheric emissions: Monitoring of pollution (TEMPO). *Journal of Quantitative Spectroscopy and Radiative Transfer*, *186*(2017), 17–39. https://doi.org/10.1016/j.jqsrt.2016.05.008